(NASA-CR-169665) TURBULENT TRANSPORT
MODELING OF SHEAR FLOWS AROUND AN
AERODYNAMIC WING. DEVELOPMENT OF TURBULENT
NEAR-WALL MODEL AND ITS APPLICATION TO
RECIRCULATING FLOWS Semiannual (Wisconsin

N83-14069

Unclas
G3/02 02259

Mechanical Engineering Department
University of Wisconsin--Milwaukee
Milwaukee, Wisconsin 53201

TURBULENT TRANSPORT MODELING OF SHEAR FLOWS AROUND AN AERODYNAMIC WING

Semi-Annual Progress Report No. 1

Development of Turbulent Near-Wall Model and Its Application to Recirculating Flows

by

R. S. Amano
Principal Investigator

The report documents research completed during the period of June 1 thru December 1, 1982 under NASA-Ames Research Grant No. NAG 2-160.

TM/82/1

ABSTRACT

The report outlines progress in implementing and refining two near-wall turbulence models in which the near-wall region is divided into either two or three zones. These models were successfully applied to the computation of recirculating flows. The research was further extended to obtaining experimental results of two different recirculating flow conditions in order to check the validity of the present models. Two different experimental apparatuses were set up: axisymmetric turbulent impinging jets on a flat plate, and turbulent flows in a circular pipe with an abrupt pipe expansion. It is shown that generally better results are obtained by using the present near-wall models, and among the models the three-zone model is superior to the two-zone model.

TABLE OF CONTENTS

NOMENCLATURE

C_μ, C_1, C_2, C_ℓ	coefficients in turbulence model
D	nozzle diameter or diameter of pipe downstream from expansion
E	empirical constant in logarithmic law
H	nozzle-to-plate distance or step height $(= (D - d)/2)$
h	heat transfer coefficient
k	turbulent kinetic energy $(\overline{u}_i^2/2)$
L	nozzle length or length of the pipe upstream from expansion
Nu	Nusselt number
P	turbulence energy generation rate
p	pressure
Re_D	Reynolds number based on diameter of pipe downstream from expansion/nozzle diameter
r	radial coordinate
T	temperature
T_w	wall temperature
T_f	fluid temperature
U	mean velocity in x direction
U_τ	friction velocity $(= \sqrt{\tau_w/\rho})$
U^+	dimensionless velocity (U/U_τ)
u, v, w	turbulent fluctuating velocities
V	mean velocity in r direction
x	coordinate parallel to flow
y	distance from wall
y^+	dimensionless distance $(= yU_\tau/\nu)$

Γ_{eff}	effective diffusivity
ε	dissipation rate of turbulence energy (= $\nu(\frac{\overline{\partial u_i}}{\partial x_j})^2$)
κ	von Karman constant
μ	dynamic viscosity
μ_{eff}	effective viscosity (= $\mu + \mu_t$)
μ_t	turbulent dynamic viscosity
ν_t	turbulent kinematic viscosity (= μ_t/ρ)
ρ	density
σ	Prandtl number
σ_k, σ_ε, σ_T	turbulent Prandtl numbers for diffusion of k, ε, and temperature
τ	turbulent shear stress
ϕ	dependent variable

Subscripts

B	values at the edge of buffer layer
E, N, S, W	values at east, north, south, and west node points
e, n, s, w	values of the cell boundaries--east, north, south, and west sides
F	values in the fully turbulent region
k, ε	values pertaining to kinetic energy and dissipation rates, respectively
P	values at node point P
t	turbulent values of quantity
v	values at the edge of viscous sublayer
w	wall values

1. INTRODUCTION

Many real flows of engineering interest contain regions of highly turbulent flow which exhibit separated, reattached, and recirculating flows even though the flow field is nominally steady overall. Aerodynamic engineers are interested in the influence of these flows on the heat and momentum characteristics on the wall boundary of airfoils, fluid machinery, blades, etc. It is frequently observed that the disturbance in the main stream usually has a significant effect on the wall boundary. This fact is usually seen in the situation of the flow in a pipe with a sudden expansion in which the separated flow reattached on the larger pipe wall and causes high heat/mass transfer rates. As another example, if we look at the turbulent jets when these impinge on a flat plate or body, it is also observed that the shear stress or heat transfer coefficient on the wall within the impingement region is significantly influenced by the turbulence intensity in the jet. This second example depicts the influence of the disturbance in the main stream on the heat, mass, and momentum characteristics on the wall. Therefore, considerable care must be taken for the evaluation of the wall-proximity region in handling the computational method. Generally, the near-wall region is divided into a viscous-affected region and a strongly turbulent region. Although the thickness of this near-wall region is usually two or more orders of magnitude less than the overall width of the flow, its effects extend over the whole flow field since, typically, 50% of the velocity change from the wall to the main stream occurs in this region.

Generally, there are two methods of accounting for these wall-proximity region in numerical methods for computing turbulent flow: the wall-function method and the low-Reynolds number modeling method. The former has some advantages: it is economical since computer time and storage required are much less than those required in the latter; it allows the introduction of additional empirical information; and it produces relatively accurate results by using fewer node points within the boundary layer compared with the low-Reynolds number modeling method, since the wall effect is evaluated only in the numerical cells next to the wall. However, the incorporation of complete wall-function in the wall adjacent cells requires enormous algebraic manipulation when many complicated equations are to be solved, such as the Algebraic Stress Model or Reynolds Stress Model.

In this report the wall-function method was adopted to the $k \sim \varepsilon$ turbulence model and near-wall models were developed for both the k and ε equations. The reasons for the adoption of the $k \sim \varepsilon$ model are (i) it is generally recognized as a reliable model, (ii) it is relatively simple compared with multi-equation models of higher-order closures, and (iii) it is still used by many aerodynamic researchers since the $k \sim \varepsilon$ model produces results as good as those obtained using Algebraic Stress Models when applied to a compressible flow.

Although the turbulence model is formulated carefully, sometimes predictions cannot be improved because of the numerical method used. The numerical model which is employed needs to be reviewed as well as turbulence models since the errors could be accumulated by numerical method per se. It is imperative to employ a numerical method which produces not only stable solutions but also accurate results. For example, the hybrid scheme of central and upwind developed by Gosman et al. [1] has been used by many researchers for a decade because of its excellent stability and simplicity when applied to turbulent flows. Despite the advantages of this hybrid scheme, it cannot give accurate results especially near the region of cell Reynolds numbers being equal to 2. Near this region, the diffusive quantities are suppressed which results in a large discrepancy between this predicted value compared to the analytical solution for a one-dimensional flow case. Consequently, the merit of higher-order closure turbulence models is easily shielded. Considering these points, a new numerical method was also developed in this report and was compared with the hybrid scheme.

Many computations were made for two types of recirculation flows: turbulent impinging jets on a flat plate, and turbulent flows in a circular pipe with a sudden expansion. For the aim of validation tests of the present computational and turbulence model, experiments were performed for these two recirculating flows.

2. NUMERICAL METHOD

2.1 Governing Equations

The present work is based on the numerical solution of the axisymmetric two-dimensional form of the time-averaged continuity, Navier-Stokes and the high Reynolds number version of $k \sim \varepsilon$ turbulence equations. The equations following this approach for the present flow configuration can be written in the following general form:

$$\frac{1}{r}\left[\frac{\partial}{\partial x}(r\rho U\phi) + \frac{\partial}{\partial r}(r\rho V\phi)\right]$$

$$= \frac{1}{r}\left[\frac{\partial}{\partial x}\left(r\Gamma_{eff}\frac{\partial\phi}{\partial x}\right) + \frac{\partial}{\partial r}\left(r\Gamma_{eff}\frac{\partial\phi}{\partial r}\right)\right] + S_{\phi} \qquad (1)$$

where ϕ stands for different dependent variables (U, V, k and ε) for which the equations are to be solved. All the equations used in this report are summarized in Table 1.

2.2 Numerical Solution Procedure

The control volume approach was adopted for solving Eq. (1) in the finite difference scheme. The grid system used in this program is a so-called staggered grid system in which the value of each scalar quantity is associated with every grid node (i.e., the points where the grid lines intersect), although the vector quantities (velocity components) are displaced in space relative to the scalar quantities. This grid system has advantages in solving the velocity field since the pressure gradients are easy to evaluate and velocities are conveniently located for the calculation of convective fluxes.

The finite difference scheme used in this paper is a method derived by expanding the exponential finite difference scheme of Spalding [2]. This scheme can be shown in the following form if Eq. (1) is written in a finite difference form.

$$A_P \phi_P = A_E \phi_E + A_W \phi_W + A_N \phi_N + A_S \phi_S + b \tag{2}$$

where

$$A_E = D_e\, f(|R_e|) + \max\{-F_e, 0\}$$

$$A_W = D_w\, f(|R_w|) + \max\{F_w, 0\}$$

$$A_N = D_n\, f(|R_n|) + \max\{-F_n, 0\}$$

$$A_S = D_s\, f(|R_s|) + \max\{F_s\ , 0\}$$

$$A_P = A_E + A_W + A_N + A_S$$

$$b = S_\phi\ \delta Vol$$

$$f(|R|) = \max\{0,\ 1 - \frac{1}{2}|R| + \frac{1}{12}|R|^2 - \frac{1}{720}|R|^4\} \tag{3}$$

$$D = \Gamma_{eff}/\delta x$$

$$F = \rho U$$

$R = F/D =$ cell Reynolds number

The function $f(|R|)$ shows the curve as in Fig. 1 in which the hybrid and the exponential schemes are compared with the present scheme. The nature of the hybrid scheme is such that it is identical with the central difference scheme for the cell Reynolds number range $-2 \leq R \leq 2$, and outside this range it reduces to the upwind difference scheme in which diffusion has been set equal to zero. However, as can be seen in Fig. 1, the departure of the hybrid scheme from the exact solution (exponential scheme) is rather large at $R \approx \pm 2$; also, it seems rather premature to set the diffusion effects equal to zero as soon as $|R|$ exceeds 2. Considering the shortcomings of the exponential scheme, i.e., exponentials are expensive to compute and the scheme is not exact for two- or three-dimensional situations, the above expression of Eq. (2) is obtained by expanding the exponential expression to the fourth order term. This scheme is not particularly expensive to compute compared to the exponential scheme. Note that this scheme reduces to the upwind differencing for $|R|$ greater than 4. Furthermore, accuracy has been improved in the range $1 < |R| < 4$.

3. TURBULENCE NEAR-WALL MODEL

3.1 Near-Wall Two-Zone Model

While viscous effects on the energy-containing turbulence motions are negligible throughout most of the flow, the no-slip condition at a solid interface always ensures that, in the immediate vicinity of a wall, viscous effects will be influential. Although the thickness of this viscous-affected zone is usually two or more orders of magnitude smaller than the overall width of the flow, its effects extend over the whole flow field since, typically, 50% of the velocity change from the wall to the free stream occurs in this region.

The near-wall model which evaluates the mean generation rate and mean dissipation rate in the k-equation in the control volume cell adjacent to the wall was proposed by Chieng and Launder [3]. This model was applied to the computation of a turbulent impinging jet by Amano and Neusen [4]. In this model, as can be seen in Fig. 2, a parabolic variation of the turbulent kinetic energy is assumed which corresonds to linear increase of fluctuating velocity with distance from the wall within the viscous sublayer. The turbulent kinetic energy, k, varies linearly towards the outer node points. The turbulent shear stress is zero within the viscous sublayer, and the shear stress undergoes an abrupt increase at the edge of the sublayer while varying linearly over the remainder of the cell. The details of this treatment of k-equation are given in reference [3]. However, these local variations of turbulent quantities were not incorporated in the evaluation of both generation and destruction terms of the ε-equation, but the value of ε in the near-wall cell was approximated under local equilibrium conditions as:

$$\varepsilon = k_p^{3/2}/C_\ell y$$

where k_P is the value of turbulent kinetic energy at the node point P adjacent to the wall.

In the present study, the treatment of the ϵ-equation in the near-wall cell is developed taking into consideration that the value of ϵ near the wall is an order of magnitude larger than that in the fully turbulent core and reaches its maximum at the wall. Each term in the ϵ-equation should be evaluated in accordance with the k-equation rather than being approximated under local equilibrium conditions. The procedure of developing the two-zone, near-wall model is described herein. The two-zone model is defined to be the one in which the near-wall region is divided into two distinct regions: a viscous sublayer region ($0 < y^+ < 11$), and a fully turbulent region ($11 < y^+ < 400$). Now, noting that we have the relation near the wall [5]:

$$k \approx 3.5\, U_\tau^2$$

or

$$k^{1/2} \approx C_\mu^{-1/4}\, U_\tau$$

If we define the Reynolds number based on the turbulence energy at the edge of viscous sublayer

$$R_v = \frac{\rho k_v^{1/2} y_v}{\mu} \tag{3}$$

then R_v is found to be 20 which corresponds to $y_v^+ = 11.0$

In the viscous sublayer and in the fully turbulent region, turbulence energy, k, energy dissipation rate, ϵ, and turbulent shear stress, τ, are expressed as follows:

(i) Viscous sublayer

$$k = k_v \left(\frac{y}{y_v}\right)^2$$

$$\epsilon = 2\nu \left(\frac{\partial k^{1/2}}{\partial y}\right)^2 \tag{4}$$

$$\tau = 0$$

(ii) Fully turbulent region

$$k = \frac{k_n - k_v}{y_n - y_v}\, y + \left(k_P - \frac{k_P - k_N}{y_P - y_N}\, y_P\right)$$

$$= by + a \tag{5}$$

$$\epsilon = k^{3/2}/C_\ell y$$

$$\tau = \tau_w + (\tau_n - \tau_w)\,\frac{y}{y_n}$$

where

$$a = k_P - \frac{k_P - k_N}{y_P - y_N}\, y_P$$

and

$$b = \frac{k_n - k_v}{y_n - y_v}$$

In the above equations, the notations in Fig. 2 are used.

The terms in the ϵ-equation represent a ϵ-balance involving convective transport, diffusion, generation, and destruction of ϵ (see both

Eq. (1) and Table 1). The convective and the diffusive terms are of minor influence near the wall and are neglected toward the wall. This fact is assured in the expression of k and ε given in Eq. (4) as:

$$\left.\frac{\partial k}{\partial y}\right|_W = 0 \quad , \left.\frac{\partial \varepsilon}{\partial y}\right|_W = 0$$

which corresponds to no diffusion of k and ε to the wall. The diffusional flux of energy dissipation out of the cell at its north, west, and east boundaries (in Fig. 2) are handled by the same differencing scheme that is employed over the remainder of the flow region.

The mean generation and destruction rate in the ε-equation can be obtained as follows: Over the fully turbulent region, the main velocity parallel to the wall is assumed to vary with distance from the wall according to

$$\frac{Uk_V^{1/2}}{\tau_W/\rho} = \frac{1}{\kappa^*} \log\,(E^* y k_V^{1/2}/\nu) \tag{6}$$

where $\kappa^* = \kappa\, C_\mu^{1/4}$ and $E^* = E\, C_\mu^{1/4}$ and κ and E are the von Karman constants.

The generation rate of k can be written as:

$$P = \tau\left(\frac{\partial U}{\partial y} + \frac{\partial V}{\partial x}\right)$$

where τ = turbulent shear stress.

Since the turbulent shear stress is zero within the viscous sublayer, by using Eqs. (5) and (7) the mean generation rate of ε can be expressed as:

$$\overline{\left(C_1\, \frac{\varepsilon}{k}\, P\right)} = \frac{1}{y_n}\int_{y_V}^{y_n} C_1\, \frac{(by + a)^{1/2}}{C_\ell y} \left[\tau_W + (\tau_n - \tau_W)\,\frac{y}{y_n}\right]\left(\frac{\partial U}{\partial y} + \frac{\partial V}{\partial x}\right) dy \tag{8}$$

By using Eq. (6) for the main velocity distribution, we can obtain the mean generation rate of ε as:

$$\overline{(C_1 \frac{\varepsilon}{k} P)} = \frac{\tau_w}{\rho} \frac{C_1}{k_v^{1/2} \kappa^* C_\ell y_n} [\tau_w(\frac{k_v^{1/2}}{y_v} - \frac{k_n^{1/2}}{y_v} + \frac{b}{2} \lambda)$$

$$+ \frac{\tau_n - \tau_w}{y_n} \{2(k_n^{1/2} - k_v^{1/2}) + a\lambda\}] + \frac{C_1}{C_\ell y_n} [\tau_w \{2(k_n^{1/2} - k_v^{1/2}) + a\lambda\}$$

$$+ \frac{2}{3} \frac{\tau_n - \tau_w}{y_n} \frac{1}{b} (k_n^{3/2} - k_v^{3/2})] \frac{\partial V}{\partial x}$$

where

$$\lambda = \begin{cases} \dfrac{1}{a^{1/2}} \log [\dfrac{(k_v^{1/2} - a^{1/2})(k_v^{1/2} + a^{1/2})}{(k_v^{1/2} - a^{1/2})(k_n^{1/2} + a^{1/2})}] & (a > 0) \\ \\ \dfrac{2}{(-a)^{1/2}} [\tan^{-1} (\dfrac{k_n}{-a})^{1/2} - \tan^{-1} (\dfrac{k_v}{-a})^{1/2}] & (a < 0) \end{cases} \tag{10}$$

Unlike the generation rate of ε, the destruction rate of ε is not zero in the viscous sublayer. In the viscous sublayer, by using Eq. (4), the average value of k can be obtained as:

$$\frac{1}{y_v} \int_0^{y_v} k dy = \frac{k_v}{3} \tag{11}$$

and the mean destruction rate is expressed as:

$$\overline{(C_2 \frac{\varepsilon^2}{k})} = C_2 \frac{12\nu^2 k_v}{y_v^3 \quad y_n} = C_2 \frac{12}{y_n y_v} (\frac{k_v}{R_v})^2 \tag{12}$$

where R_v is defined in Eq. (3).

To evaluate the destruction rate in the fully-turbulent region, we integrate $(C_2\varepsilon^2/k)$ between y_v and y_n. After including the linear variation of k in Eq. (5) and the contribution of destruction in the viscous sublayer given in Eq. (12), the mean rate can be given as:

$$\overline{(C_2 \frac{\varepsilon^2}{k})} = C_2 \left\{ \frac{12}{y_n y_v} (\frac{k_v}{R_v})^2 + \frac{1 - y_v/y_n}{C_\ell^2} (\frac{a^2}{y_v y_n} + \frac{2ab}{y_n - y_v} \log \frac{y_n}{y_v} + b^2) \right\} \tag{13}$$

where a and b are given in Eq. (5). The near-wall two-zone model described above is summarized in Table 2.

3.2 Near-Wall Three-Zone Model

In the previous section, we developed the approximation of near-wall region by dividing the region into two distinct zones. However, most of the experimental data show [6 and 7, for example] that both the linear and logarithmic profiles deviate from the experimental data in the buffer zone, as shown in Fig. 3. Therefore, in this section, a three-zone near-wall model is proposed which is comprised of a viscous sublayer ($0 < y^+ < 5$) adjacent to the wall, a buffer zone ($5 < y^+ < 30$), and a fully turbulent zone ($30 < y^+ < 400$).

Figure 4(a) shows a computational node P whose associated control volume is bounded on the south side by a wall. In this figure the three zones are shown such that the node point P lies outside the buffer zone assuming the near-wall cell is large enough. However, the computer program self adjusts the cases when P lies in either buffer zone or viscous sublayer. The behavior of the turbulent kinetic energy, k, and the turbulent shear stress, τ, needs to be proposed especially in the viscous sublayer and the buffer zone. Bakewell and Lumley [8] reported that the streamwise fluctuating velocity increases linearly with distance from the wall, y, within the viscous sublayer and then it increases with y^n in the outer region of the viscous sublayer. These data are plotted in Fig. 5. Hence, as we have done in the previous section, k is assumed to vary in a parabolic profile within the viscous sublayer. If we examine the slope of the fluctuating velocities in Fig. 5, the powers n of the fluctuating velocities in three directions fall in the range between 0.175 to 1.175 within the buffer zone. The average of the values n shows approximately 0.7. However, we assumed that n is approximately 0.5 which gives more insight by losing little accuracy, since $u \sim y^{0.5}$ indicates $k \sim y$, i.e., linear approximation of k within the buffer zone. Within the fully turbulent region, the variation of k is controlled by the methodology of finite difference and the linear variation between node P and its northern neighbor is applied to extrapolate to the edge of the buffer layer (see Fig. 4(b)).

Unlike the variation of k, the turbulent shear stress τ has a different dependence on y. If the streamwise velocity has a relation $U \sim y$ near the wall, then, from the continuity equation, it is deduced that $V \sim y^2$ and the convective acceleration is proportional to y^2. Hence, we have

$$\frac{\partial}{\partial y}\left(\mu_t \frac{\partial U}{\partial y}\right) \sim y^2$$

or $$\tau \sim t^3.$$

This cubic profile generally yields very small values of τ within the viscous sublayer, which thus permits τ to be treated as negligible in this viscous sublayer. While in the buffer zone, τ is assumed to vary with cubic profile and undergoes a relatively sharp increase at the edge of the buffer layer and varies linearly over the remainder of the cell. This approximation, shown in Fig. 4(c), again gives more insight since, by setting $\tau = 0$ within the viscous sublayer, algebraic expressions can be simplified considerably with little loss of accuracy.

From the above discussion, the variation of k, ε and τ can be summarized in the following form in the three zones.

(i) Viscous sublayer

$$k = k_V \left(\frac{y}{y_V}\right)^2$$

$$\varepsilon = 2\nu\left(\frac{\partial k^{1/2}}{\partial y}\right)^2 \tag{14}$$

$$\tau = 0$$

(ii) Buffer layer

$$k = k_B \frac{y}{y_B}$$

$$\varepsilon = k^{3/2}/C_\ell y \tag{15}$$

$$\tau = \tau_B \left(\frac{y}{y_B}\right)^3$$

(iii) Fully turbulent region

$$k = \frac{k_n - k_B}{y_n - y_B}\, y + \left(k_P - \frac{k_P - k_N}{y_P - y_N}\, y_P\right)$$

$$= by + a \tag{16}$$

$$\varepsilon = k^{3/2}/C_\ell y$$

$$\tau = \tau_w + (\tau_n - \tau_w)\,\frac{y}{y_n}$$

where

$$a = k_P - \frac{k_P - k_N}{y_P - y_N}\, y_P$$

$$b = \frac{k_n - k_B}{y_n - y_B}$$

In Eqs. (14) - (16), the notations in Fig. 4 are used.

The mean values of generation and destruction rates for both k and ε equations are obtained by integrating the local variables of generation (P and $C_1 P\varepsilon/k$) and destruction (ε and $C_2\varepsilon^2/k$) over the computational cell after inserting the relations in Eqs. (14) - (16) and then dividing by the volume of the cell. The streamwise velocity in the fully turbulent region can be given the following form.

$$\frac{U k_B^{1/2}}{\tau_w/\rho} = \frac{1}{\kappa^*} \ln\left(E^* \, y\, k_B^{1/2}/\nu\right) \tag{17}$$

where E^* and κ^* are defined in Eq. (16).

(i) The mean generation rate of the k-equation, $\overline{P}$:

The generation rate, P, can be approximated as:

$$P = \tau\left(\frac{\partial U}{\partial y} + \frac{\partial V}{\partial x}\right) \tag{18}$$

Thus,

$$\overline{P} = \frac{1}{y_n}\left[\int_{y_v}^{y_B} \tau_B\left(\frac{y}{y_B}\right)^3 \left(\frac{\partial U}{\partial y} + \frac{\partial V}{\partial x}\right)_B dy\right.$$

$$\left. + \int_{y_B}^{y_n} \left\{\tau_w + (\tau_n - \tau_w)\frac{y}{y_n}\right\} \left(\frac{\partial U}{\partial y} + \frac{\partial V}{\partial x}\right)_F dy\right] . \tag{19}$$

By using Eq. (17) for the second term in Eq. (19), we can obtain the following form:

$$\overline{P} = \frac{\tau_w(U_n - U_B)}{y_n} + \frac{\tau_B}{4y_B^3 y_n}(y_B^4 - y_v^4)\left(\frac{\partial U}{\partial y}\right)_B$$

$$+ \frac{\tau_w(\tau_n - \tau_w)}{\rho\kappa^* k_B^{1/2} y_n}\left(1 - \frac{y_B}{y_n}\right) \tag{20}$$

$$+ \left[\tau_w\left(1 - \frac{y_B}{y_n}\right) + \frac{\tau_n - \tau_w}{2}\left\{1 - \left(\frac{y_B}{y_n}\right)^2\right\}\right]\left(\frac{\partial V}{\partial x}\right)_F$$

in which $(\partial V/\partial x)_B$ is assumed to be negligible.

(ii) The mean dissipation rate of the k-equation, $\overline{\varepsilon}$

$$\overline{\varepsilon} = \frac{1}{y_n} [\int_0^{y_v} \varepsilon_v \, dy + \int_{y_v}^{y_B} \varepsilon_B \, dy + \int_{y_B}^{y_n} \varepsilon_F \, dy] \tag{21}$$

where the subscripts v, B, and F stand for viscous sublayer, buffer layer, and fully turbulent region, respectively. After substituting Eqs. (14) - (16) into Eq. (21), we obtain

$$\overline{\varepsilon} = \frac{2k_v^{3/2}}{y_n R_v} + \frac{1}{y_n C_\ell} [\frac{2}{3} k_B^{3/2} \{1 - (\frac{y_v}{y_B})^{3/2}\} \tag{22}$$

$$+ \frac{2}{3} (k_n^{3/2} - k_B^{3/2}) + 2a(k_n^{1/2} - k_B^{1/2}) + a^2 \lambda]$$

where

$$\lambda = \begin{cases} \dfrac{1}{a^{1/2}} \log [\dfrac{(k_n^{1/2} - a^{1/2})(k_B^{1/2} + a^{1/2})}{(k_B^{1/2} - a^{1/2})(k_n^{1/2} + a^{1/2})}] & (a > 0) \\ \\ \dfrac{2}{(-a)^{1/2}} \tan^{-1} (\dfrac{k_n}{-a})^{1/2} - \tan^{-1} (\dfrac{k_B}{-a})^{1/2}] & (a < 0) \end{cases}$$

and where a and b are given in Eq. (16).

(iii) The generation rate of the ε-equation $\overline{C_1 P \varepsilon/k}$:

By using the expression in Eq. (18), we obtain as:

$$\overline{C_1 \frac{\varepsilon}{k} P} = \frac{C_1}{y_n} \int_{y_v}^{y_B} \frac{\varepsilon}{k} \tau \left(\frac{\partial U}{\partial y} + \frac{\partial V}{\partial x}\right)_B dy$$

$$+ \int_{y_B}^{y_b} \frac{\varepsilon}{k} \tau \left(\frac{\partial U}{\partial y} + \frac{\partial V}{\partial x}\right)_F dy \tag{23}$$

and substituting Eqs. (14) - (17),

$$\overline{C_1 \frac{\varepsilon}{k} P} = \frac{C_1}{C_\ell y_n} \Big[\frac{2}{7} \tau_B k_B^{1/2} \{1 - (\frac{y_v}{y_B})^{7/2}\} (\frac{\partial U}{\partial y})_B$$

$$+ \frac{\tau_w}{\rho k_B^{1/2} \kappa^*} \{\tau_w (\frac{k_B^{1/2}}{y_B} - \frac{y_n^{1/2}}{y_n} + \frac{b}{2} \lambda) \qquad (24)$$

$$+ \frac{\tau_n - \tau_w}{y_n} (2(k_n^{1/2} - k_B^{1/2}) + a\lambda)\}$$

$$+ \{\tau_w (2(k_n^{1/2} - k_B^{1/2}) + a\lambda) + \frac{2}{3} \frac{\tau_n - \tau_w}{y_n} \frac{1}{b} (k_n^{3/2} - k_B^{3/2})\} \frac{\partial V}{\partial x}\Big]$$

(iv) The mean destruction rate of the ε-equation, $\overline{C_2 \varepsilon^2/k}$:

$$\overline{C_2 \frac{\varepsilon^2}{k}} = \frac{C_2}{y_n} \Big[\int_0^{y_v} (\frac{\varepsilon^2}{k})_v \, dy + \int_{y_v}^{y_B} (\frac{\varepsilon^2}{k})_B \, dy + \int_{y_B}^{y_n} (\frac{\varepsilon^2}{k})_F \, dy\Big] \qquad (25)$$

Since the k value has a singular point at y = 0, we approximate the integration within the viscous sublayer as we did in the two-zone model (see Eq. (11)). Then after substituting Eqs. (14) - (16), we obtain:

$$\overline{C_2 \frac{\varepsilon^2}{k}} = C_2 \Big[\frac{12}{y_n y_v} (\frac{k_v}{R_v})^2 + (\frac{k_B}{C_\ell})^2 \frac{1}{y_B y_n} (1 - \frac{y_v}{y_B})$$

$$+ \frac{1 - y_B/y_n}{C_\ell^2} (\frac{a^2}{y_B y_n} + \frac{2ab}{y_n - y_B} \log \frac{y_n}{y_B} + b^2)\Big] \qquad (26)$$

All the results developed above are summarized in Table 3.

4. EXPERIMENTAL APPARATUS AND PROCEDURE

4.1 Turbulent Jets Impinging on a Flat Plate

Experimental heat transfer coefficients were obtained by using an electrically-heated flat plate with an axisymmetric air jet impinging normally to the surface of the plate (Fig. 6). Nozzle-to-plate spacing, distance from the nozzle centerline, and nozzle Reynolds number were varied so that the heat transfer characteristics of this configuration could be determined over a range of conditions.

The test section was located in a large transparent enclosure to ensure that air movement within the room did not affect the tests. Holes in the top of this enclosure allowed heated air to escape; thus, the temperature within this enclosure did not vary appreciably during tests. The electrical power used to establish the uniform wall heat flux boundary condition was supplied by a DC power supply (1% ripple). The air flow rate was measured with a calibrated rotameter. Air and wall temperatures were measured with copper-constantan thermocouples. Thermocouple voltages, test-section voltage drop, and the voltage drop across the calibrated shunt, which was used to measure the current flow through the test section, were measured with a digital voltmeter.

The test section consisted of a thin (0.81 mm) stainless steel plate with the heated portion being approximately 15 cm by 15 cm (see Fig. 7). Copper bus bars were soldered to both ends of the plate to ensure a uniform voltage drop along the test section. The electric resistance heating resulted in a uniform wall heat flux. The plate was mounted on a transite block, and its back and sides were heavily insulated to minimize conduction losses. Five thermocouples were mounted to the back of the plate 2.5 cm apart along one diagonal of the test section and centered at the intersection of the two diagonals. A sixth thermocouple was located 5.0 cm from the center of the plate on the other diagonal. This arrangement permitted the symmetry of the jet to be checked by examination of the heat transfer coefficients.

The nozzle consisted of a circular stainless steel tube 4.6 mm I.D. and L/D = 75. A smooth plastic tube with a slightly larger I.D. than that of the nozzle connected the flow meter to the nozzle. The long nozzle length ensured a fully-developed velocity profile of the nozzle exit. The jet air temperature was measured with a thermocouple which was located in the plastic tube approximately 50 cm from the entrance to the nozzle.

Before the electrical power was applied to the test section, the nozzle was positioned perpendicularly above the plate, at a specified H/D value at the intersection of the two diagonals where a thermocouple was located. The symmetry of the resulting flow was checked in two ways. Prior to heating the plate, a velocity impact probe was used to measure jet velocities about 3 mm above the plate surface and 2.5 and 5 mm from the nozzle centerline along the two diagonals. This procedure confirmed a generally symmetric flow pattern, but indicated a slight instability in the flow which caused a small random shifting of the flow pattern. The symmetry was also checked by examining the heat transfer coefficients. This inspection also confirmed the symmetric flow pattern. After data were taken at one position, the nozzle was shifted laterally for a distance of one nozzle diameter along the diagonal and additional data were taken.

Heat transfer data were taken after the power was turned on and steady state conditions (as indicated by temperature measurements) were obtained on the test section. For each test run, the air flow was set to a specified level and was kept at this value through the run. The flow rate was very steady. Test section power was set to a level such that the temperature difference between the wall thermocouple at the jet stagnation point and the jet temperature was about 15K. The power was kept at this value throughout the runs at a set Reynolds number and H/D ratio.

The heat flux from the test section wall was calculated using the voltage drop across the test section wall and the current flowing through it. To calculate the outer wall temperature, utilizing the experimentally measured inner wall temperature and the heat generation rate, the steady-state differential conduction equation for a plane wall was solved, assuming one-dimensional heat flow and constant thermophysical properties of the steel. Radiation from the test section was estimated and found to have a negligible effect. Heat transfer coefficients were calculated using the wall heat flux, outer wall temperature and jet temperature.

Data were taken at H/D = 4, 7, and 10, Reynolds numbers at 10^4, 2×10^4, and 4×10^4 and $-12 \leq r/D \leq 22$. Heat fluxes of 1950 to 8200 w/m were used, which resulted in temperature differences $(T_w - T_f)$ of 15K to 75K. Uncertainties in the experimental quantities are estimated to be: q", ± 2%; Re_D, ± 3%; and h, ± 5%.

4.2 Turbulent Flows in a Circular Pipe with an Abrupt Pipe Expansion

To determine the heat transfer characteristics downstream of a circular abrupt expansion, three test sections were tested over a wide range of Reynolds numbers. The test sections were placed vertically in a flow loop, a schematic of which is shown in Fig. 8. Liquid R-113 was pumped through the test sections at predetermined flow rates by adjusting the amount of fluid allowed to bypass the flow loop. The inlet temperature to the test section was controlled by adjusting the electric preheater power. High pressure maintained single-phase flow throughout the test section. The flow was measured with calibrated rotameters. Fluid and wall temperatures were obtained with copper-constantan thermocouples.

The test section (See Fig. 9) was constructed from a 12.2mm I.D., 457mm long stainless steel tube. A uniform wall heat flux was obtained by passing a DC current through the tube. The wall thickness of 0.254mm helped to minimize axial conduction. Brass bus bars were silver soldered to each end of the tube. A thick layer of insulation reduced heat losses to a negligible level. Thirty thermocouples were spaced along the outside tube wall, including three on the inlet bus bar to help evaluate the effect of the axial conduction. The first 19 thermocouples were spaced 4.76mm apart; the next four were spaced 12.7mm apart; and the final seven were spaced 25.4mm apart. The shorter thermocouple spacing just downstream of the expansion was necessary since relatively large variations over short distances in the heat transfer coefficients were anticipated in this area. The thermocouple voltages as well as the test section voltage drop and shunt voltage drop (from which test section current was obtained) were measured with a digital voltmeter with an accuracy of 1 μv.

The nozzles were machined from a hard plastic ("Delrin"). Nozzle diameters of 2.38mm, 4.76mm, and 7.15mm were used which resulted in expansion ratios (d/D) of 0.195, 0.391, and 0.586, respectively. The nozzle exit was perpendicular and concentric to the stainless steel tube. Total nozzle length was about $L/d \approx 50$ for all three cases so that a fully developed turbulent flow would be ensured at the nozzle exit. The entrance to the nozzle was contoured so that there was a relatively smooth transition from the 25.4mm supply piping to the nozzle.

Before any data were taken, the flow rate and inlet fluid temperature were adjusted to give a specified Reynolds number based on the tube diameter downstream of the abrupt expansion. The test section power was then adjusted so that a maximum temperature difference between the wall and the fluid never exceeded approximately 35K. At the location of the maximum heat transfer coefficient, these power settings resulted in a minimum temperature difference ranging from about 2K at $Re \approx 10^4$ to 10K at $Re \approx 1.5 \times 10^5$. The temperature rise of the fluid ranged from about 3 to 5K. After steady-state conditions were attained, the data were taken.

The inside wall temperatures were obtained using this measured outside wall temperature and the electrical power dissipation rate. The steady-state heat conduction equation with internal heat generation in cylindrical coordinates was solved by assuming one-dimensional radial conduction with constant thermophysical properties. Because of the thin tube wall, low thermal conductivity, and relatively high heat transfer coefficients, axial conduction was assumed to be small. Thus, the heat flux was calculated by dividing the total power dissipation by the inside wall area of the heated tube. The heat transfer coefficients were then calculated by dividing the heat flux by the local temperature difference $(T_w - T_f)$ at any location along the test section.

Heat balances comparing electrical dissipation with enthalpy rise of the fluid generally were within ±5%. A propagation-of-error analysis suggests that the uncertainty in the heat transfer coefficients at the point of the maximum heat transfer coefficient range from about ±4.7% for the largest d/D ratio and highest Reynolds number to about ±9.5% for the smallest d/D ratio and lowest Reynolds number. Uncertainties at other locations in the tube are smaller than these. The uncertainty in the Reynolds number is estimated to be ±2%.

5. PRESENTATION AND DISCUSSION OF RESULTS

The experimental results of the heat transfer coefficients along the flat plate for the turbulent impinging jets are shown in Figs. 10-12 for three different nozzle Reynolds numbers, Re_D, and for three nozzle-to-plate distances, H/D. These data show smoothly decreasing heat transfer coefficients with increasing distance from the stagnation point along the flat plate. The heat transfer coefficient also increases with increasing Re_D and decreasing H/D.

As comparisons of these data with the numerical model, the near-wall two-zone model developed in Section 3.1 was used for the computation of the heat transfer coefficients along the flat plate for these impinging jet experiments and were compared with the experimental data. These computed results were further compared with the results obtained by employing the simpler near-wall models: the two-zone model of Chieng and Launder [3] in which the two-zone is considered only for the k-equations and not for the ϵ-equations, and the one-zone model. These are shown in Figs. 13 and 14 for $H/D = 4$ and 10, respectively. For both cases the nozzle Reynolds number is 2×10^4.

Note the generally close similarity of the results for the two different H/D; in particular, the calculated results show a much steeper slope in the impingement region. Comparing the one-zone model and the simpler version of the two-zone model, the results are generally improved by approximately 30% by employing the two-zone model. Further comparison between the simpler two-zone model and the present two-zone model in which both the k and ϵ-equations are evaluated by taking the local values into consideration, it is obvious that the present effort improves the prediction, especially in the impingement regions approximately by 10%. However, the levels of heat transfer coefficients do not change in most of the regions except near the stagnation points. This indicates that the treatment of the ϵ-equation is significantly sensitive, especially in the low Reynolds number region where very fine scale eddy motions take place. Consequently, such fine scale motions directly influence the behavior of ϵ.

Next the three-zone model developed in Section 3.2 is compared with experimental data of turbulent flows in a circular pipe with an abrupt expansion. The experimental results of this flow are shown in Figs. 15-19. Figures 15-17 represent the variation of Nusselt number for different Reynolds number based on a large pipe, Re_D, and Figs. 18 and 19 represent the variation of Nusselt number for different pipe expansion ratios, d/D. For any particular test, the Nusselt number for different pipe expansion ratios, d/D. For any particular test, the Nusselt number starts at a low level, increases as one moves away from the pipe expansion section and then decreases, eventually reaching the fully developed condition in 30 to 40 pipe diameters. The maximum Nusselt number occurs about 6 to 8 step heights, H, downstream from the expansion section in all cases. The levels of Nusselt number increases with increasing Reynolds number and decreasing expansion ratio, d/D.

Figures 20-23 display comparisons of the two-zone and three-zone models with the experimental data for two different Reynolds numbers and for d/D =

0.391 and 0.586. From these results, it is easily seen that the results obtained by employing the three-zone model show surprisingly better results than those obtained with the two-zone model. Note also that by using the two-zone model the predicted maximum Nusselt numbers display 5 - 20% higher values than the experimental data for $Re_D = 2 \times 10^4$, while these predictions are 50 - 100% higher than the experimental values at $Re_D = 8 \times 10^4$ when the two-zone model was used. On the other hand the predictions of the maximum Nusselt number with the three-zone model shows differences of -20% at $Re_D = 2 \times 10^4$ and +13% at $Re_D = 8 \times 10^4$. Generally, it can be said that, by employing three-zone models, relatively better agreement with the experimental data can be obtained for a wide range of Reynolds numbers, but the two-zone model should not be used when the Reynolds numbers are greater than, say, 5×10^4, since it predicts values for the heat transfer rate which are too high.

Unlike the difference in the predicted levels of Nusselt number, the location of the predicted maximum Nusselt number does not vary with the different wall function models. Thus, it may be concluded that none of the various aspects of the wall function models developed in this study has any significant effect on the axial location of the maximum Nusselt number; the position of the maximum Nusselt number is controlled by the turbulence model per se. It is also concluded that the wall function treatment is not very important for relatively low Reynolds number flows ($Re_D < 5 \times 10^5$) but is significant for high Reynolds number flows.

6. SUMMARIZING REMARKS

The report has presented two different near-wall models developed based on the wall-functions. The principal advantage of these models, particularly the three-zone model, is that they produce wall proximity characteristics more accurately independent of the flow Reynolds numbers when applied to the recirculating flows. There are also several advantages noted in the use of these near-wall models developed here:

1. a large number of cells is not necessary to obtain relatively accurate results if the near-wall model is employed; and
2. we can improve predictions when applied to the $k \sim \varepsilon$ model with relatively little effort, etc.

It has been shown that although the three-zone model makes better predictions than the two-zone model, the latter still considerably improves the accuracy of prediction when compared with the one-zone model in which any local variations of turbulent quantities are not taken into account. Furthermore, modification of computer programs by incorporating the two-zone model is simpler than that required for the three-zone model. Therefore, when the computer program is very complicated, an adoption of the two-zone model can still improve the results.

The studies of the application of these near-wall models to the flow around an aerodynamic wing by employing the $k \sim \varepsilon$ model and the Reynolds Stress Model will be presented in the next report.

REFERENCES

1. Gosman, A. D., Pun, W. M., Runchal, A. K., Spalding, D. B. and Wolfshtein, M. Heat and Mass Transfer in Recirculating Flows, Academic Press, 1969.
2. Spalding, D. B., "A Novel Finite-Difference Formulation for Differential Expressions Involving both First and Second Derivatives," International Journal for Numerical Methods in Engineering, Vol. 4, 1972, pp. 551-559.
3. Chieng, C. C. and Launder, B. E., "On the Calculation of Turbulent Heat Transport Downstream from an Abrupt Pipe Expansion, Numerical Heat Transfer, Vol. 3, 1980, pp. 189-207.
4. Amano, R. S. and Neusen, K. F. "A Numerical and Experimental Investigation of High-Velocity Jets Impinging on a Flat Plate," Proceedings of the 6th International Symposium on Jet Cutting Technology, April 1982, pp. 107-122.
5. Hanjalic, K. and Launder, B. E., "A Reynolds Stress Model of Turbulence and Its Application to Thin Shear Flows," Journal of Fluid Mechanics, Vol. 52, Part 4, 1972, pp. 609-638.
6. Laufer, J., NACA Report No. 1174, 1954.
7. Lindgren, E. R., Oklahoma State University, Civil Engineering Department Report 1AD621071, 1965.
8. Bakewell, H. P. and Lumley, J. L., "Viscous Sublayer and Adjacent Wall Region in Turbulent Pipe Flow," Physics of Fluids, Vol. 10, 1967, p. 1880.

Table 1 Summary of Equations Solved

Equation	ϕ	Γ_{eff}	S_ϕ
Continuity	1	0	0
x-momentum	U	μ_{eff}	$-\frac{\partial p}{\partial x} + \frac{\partial}{\partial x}(\mu_{eff}\frac{\partial U}{\partial x})$ $+\frac{1}{r}\frac{\partial}{\partial r}(r\mu_{eff}\frac{\partial V}{\partial x})$
r-momentum	V	μ_{eff}	$-\frac{\partial p}{\partial r} + \frac{\partial}{\partial x}(\mu_{eff}\frac{\partial U}{\partial r})$ $+\frac{1}{r}\frac{\partial}{\partial r}(r\mu_{eff}\frac{\partial V}{\partial r})$ $-2\mu_{eff}V/r^2$
Turbulence energy	k	$\mu + \frac{\mu_t}{\sigma_k}$	$\rho P - \rho\varepsilon$
Energy dissipation	ε	$\mu + \frac{\mu_t}{\sigma_\varepsilon}$	$C_1\frac{\rho\varepsilon}{k}P - C_2\frac{\rho\varepsilon^2}{k}$

where

$$\mu_t = C_\mu \rho k^2/\varepsilon$$

and

$$P = \nu_t[(\frac{\partial U}{\partial r} + \frac{\partial V}{\partial x})^2 + 2(\frac{\partial U}{\partial x})^2 + 2(\frac{\partial V}{\partial r})^2 + 2(\frac{V}{r})^2]$$

and constants are

C_μ	C_1	C_2	σ_k	σ_ε
0.09	1.44	1.92	1.0	1.3

Table 2. Near-Wall Two Zone Model

Generation rate in k-equation $\overline{P}$

$$\frac{\tau_w(U_n - U_v)}{y_n} + \frac{\tau_w(\tau_n - \tau_w)}{\rho\kappa^* k_v^{\frac{1}{2}} y_n}\left(1 - \frac{y_v}{y_n}\right)$$

$$+ \left[\tau_w\left(1 - \frac{y_v}{y_n}\right) + \frac{\tau_n - \tau_w}{2}\left\{1 - \left(\frac{y_v}{y_n}\right)^2\right\}\right]\frac{\partial V}{\partial x}$$

Dissipation rate in k-equation $\overline{\varepsilon}$

$$\frac{2k_v^{\frac{3}{2}}}{y_n Rv} + \frac{1}{y_n C_\ell}\left[\frac{2}{3}\left(k_n^{\frac{3}{2}} - k_v^{\frac{3}{2}}\right) + 2a\left(k_n^{\frac{1}{2}} - k_v^{\frac{1}{2}}\right) + a^2\lambda\right]$$

Generation rate in ε-equation $(\overline{C_1 P\varepsilon/k})$

$$\frac{\tau_w}{\rho}\frac{C_1}{k_v^{\frac{1}{2}}\kappa^* C_\ell y_n}\left[\tau_w\left(\frac{k_v^{\frac{1}{2}}}{y_v} - \frac{k_n^{\frac{1}{2}}}{y_n} + \frac{b}{2}\lambda\right)\right.$$

$$\left. + \frac{\tau_n - \tau_w}{y_n}\left(2\left(k_n^{\frac{1}{2}} - k_v^{\frac{1}{2}}\right) + a\lambda\right)\right]$$

$$+ \frac{C_1}{C_\ell y_n}\left[\tau_w\left(2\left(k_n^{\frac{1}{2}} - k_v^{\frac{1}{2}}\right) + a\lambda\right)\right.$$

$$\left. + \frac{2}{3}\frac{\tau_n - \tau_w}{y_n}\frac{1}{b}\left(k_n^{\frac{3}{2}} - k_v^{\frac{3}{2}}\right)\right]\frac{\partial V}{\partial x}$$

Destruction rate in ε-equation $(\overline{C_2 \varepsilon^2/k})$

$$C_2\left[\frac{12}{y_n y_v}\left(\frac{k_v}{Rv}\right)^2 + \frac{1 - y_v/y_n}{C_\ell^{\,2}}\left(\frac{a^2}{y_v y_n}\right.\right.$$

$$\left.\left. + \frac{2ab}{y_n - y_v}\log\frac{y_n}{y_v} + b^2\right)\right]$$

Table 2. Near-Wall Two Zone Model - Cont.

where

$$\lambda = \begin{cases} \dfrac{1}{a^{\frac{1}{2}}} \log\left[\dfrac{(k_n^{\frac{1}{2}} - a^{\frac{1}{2}})(k_v^{\frac{1}{2}} + a^{\frac{1}{2}})}{(k_v^{\frac{1}{2}} - a^{\frac{1}{2}})(k_n^{\frac{1}{2}} + a^{\frac{1}{2}})}\right] & (a>0) \\ \dfrac{2}{(-a)^{\frac{1}{2}}}\left[\tan^{-1}\left(\dfrac{k_n}{-a}\right)^{\frac{1}{2}} - \tan^{-1}\left(\dfrac{k_v}{-a}\right)^{\frac{1}{2}}\right] & (a<0) \end{cases}$$

$$a = k_P - \frac{k_P - k_N}{y_P - y_N}\, y_P$$

$$b = \frac{k_n - k_v}{y_n - y_v}$$

Table 3. Near-Wall Three Zone Model

Generation rate in k-equation $\overline{P}$

$$\frac{\tau_w(U_n - U_B)}{y_n} + \frac{\tau_B}{4y_B^3 y_n}(y_B^4 - y_v^4)(\frac{\partial U}{\partial y})_B$$

$$+ \frac{\tau_w(\tau_n - \tau_v)}{\rho\kappa^* k_B^{\frac{1}{2}} y_n} (1 - \frac{y_B}{y_n})$$

$$+[\tau_w(1 - \frac{y_B}{y_n}) + \frac{\tau_n - \tau_w}{2}\{1 - (\frac{y_B}{y_n})^2\}]\frac{\partial V}{\partial x}$$

Dissipation rate in k-equation $\overline{\varepsilon}$

$$\frac{2k_v^{\frac{3}{2}}}{y_n R_v} + \frac{1}{y_n C_\ell}[\frac{2}{3}k_B^{\frac{3}{2}} \{1 - (\frac{y_v}{y_B})^{\frac{3}{2}}\}$$

$$+ \frac{2}{3} (k_n^{\frac{3}{2}} - k_B^{\frac{3}{2}}) + 2a(k_n^{\frac{1}{2}} - k_B^{\frac{1}{2}}) + a^2\lambda]$$

Generation rate in ε-equation $(\overline{C_1 P\varepsilon/k})$

$$\frac{2}{7} \frac{C_1 \tau_B}{C_\ell y_n} k_B^{\frac{1}{2}} \{1 - (\frac{y_v}{y_B})^{\frac{7}{2}}\} (\frac{\partial U}{\partial y})_B$$

$$+ \frac{\tau_w}{\rho} \frac{C_1}{k_B^{\frac{1}{2}}\kappa^* C_\ell y_n}[\tau_w(\frac{k_B^{\frac{1}{2}}}{y_B} - \frac{k_n^{\frac{1}{2}}}{y_n} + \frac{b}{2}\lambda)$$

$$+ \frac{\tau_n - \tau_w}{y_n}\{2(k_n^{\frac{1}{2}} - k_B^{\frac{1}{2}}) + a\lambda\}]$$

$$+ \frac{C_1}{C_\ell y_n}[\tau_w\{2(k_n^{\frac{1}{2}} - k_B^{\frac{1}{2}}) + a\lambda\}$$

$$+ \frac{2}{3} \frac{\tau_n - \tau_w}{y_n} \frac{1}{b} (k_n^{\frac{3}{2}} - k_B^{\frac{3}{2}})] \frac{\partial V}{\partial x}$$

Table 3. Near-Wall Three Zone Model - Cont.

Destruction $\overline{(C_2 \varepsilon^2/k)}$

$$C_2\left[\frac{12}{y_n y_v}\left(\frac{k_v}{Rv}\right)^2 + \left(\frac{k_B}{C_\ell}\right)^2 \frac{1}{y_B y_n}\left(1 - \frac{y_v}{y_B}\right)\right.$$

$$\left. + \frac{1 - y_B/y_n}{C_\ell{}^2}\left(\frac{a^2}{y_B y_n} + \frac{2ab}{y_n - y_B} \log \frac{y_n}{y_B} + b^2\right)\right]$$

where

$$\lambda = \begin{cases} \dfrac{1}{a^{\frac{1}{2}}} \log\left[\dfrac{(k_n{}^{\frac{1}{2}} - a^{\frac{1}{2}})(k_B{}^{\frac{1}{2}} + a^{\frac{1}{2}})}{(k_B{}^{\frac{1}{2}} - a^{\frac{1}{2}})(k_n{}^{\frac{1}{2}} + a^{\frac{1}{2}})}\right] & (a>0) \\ \\ \dfrac{2}{(-a)^{\frac{1}{2}}}\left[\tan^{-1}\left(\dfrac{k_n}{-a}\right)^{\frac{1}{2}} - \tan^{-1}\left(\dfrac{k_B}{-a}\right)^{\frac{1}{2}}\right] & (a<0) \end{cases}$$

$$a = k_P - \frac{k_P - k_N}{y_P - y_N}\, y_P$$

$$b = \frac{k_n - k_B}{y_n - y_B}$$

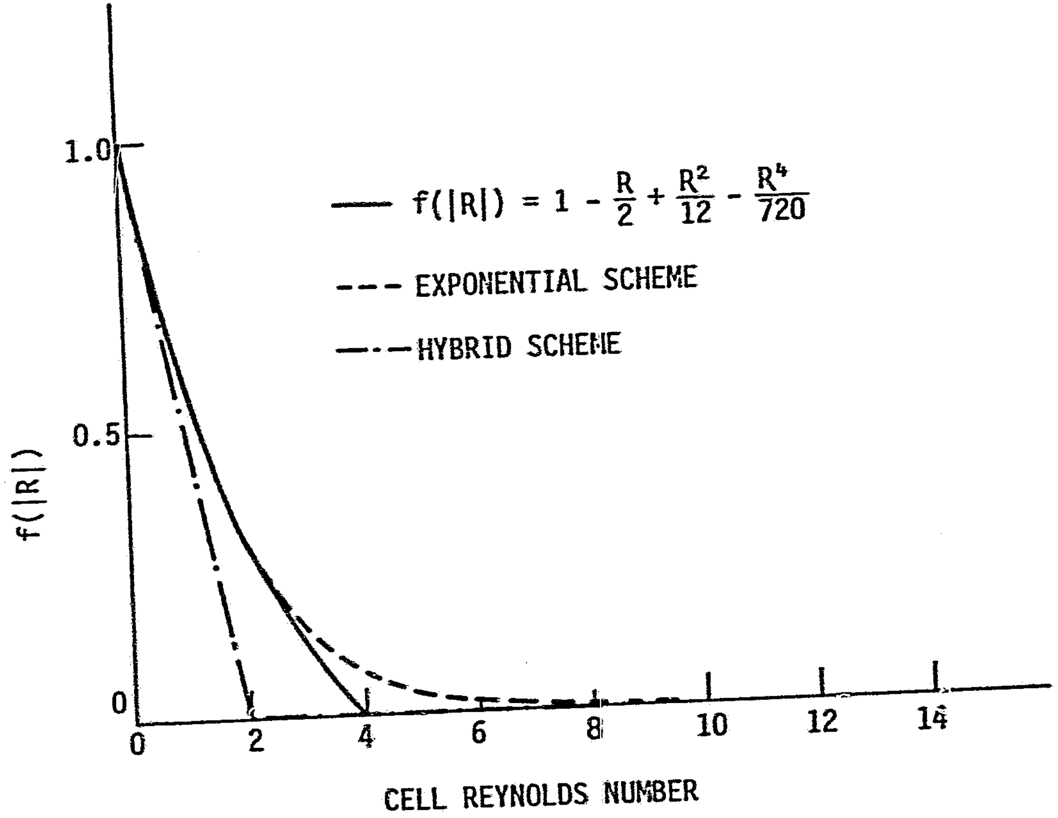

Fig. 1 The function of f(|R|) for various schemes

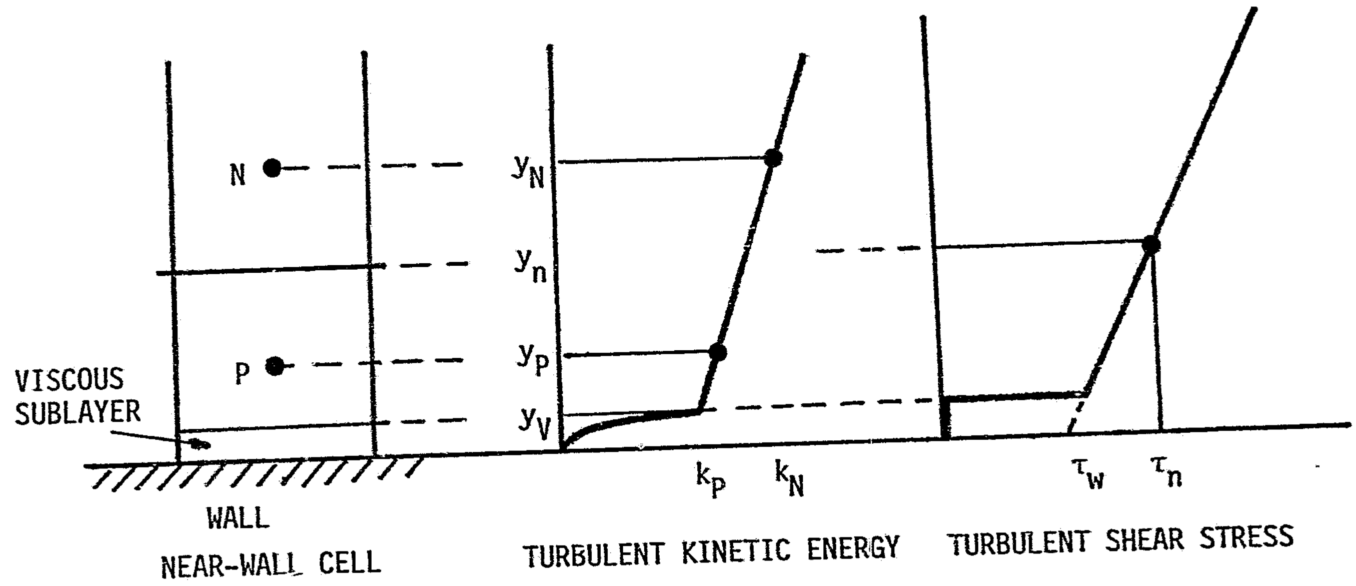

Fig. 2 Near-Wall Two-Zone Model

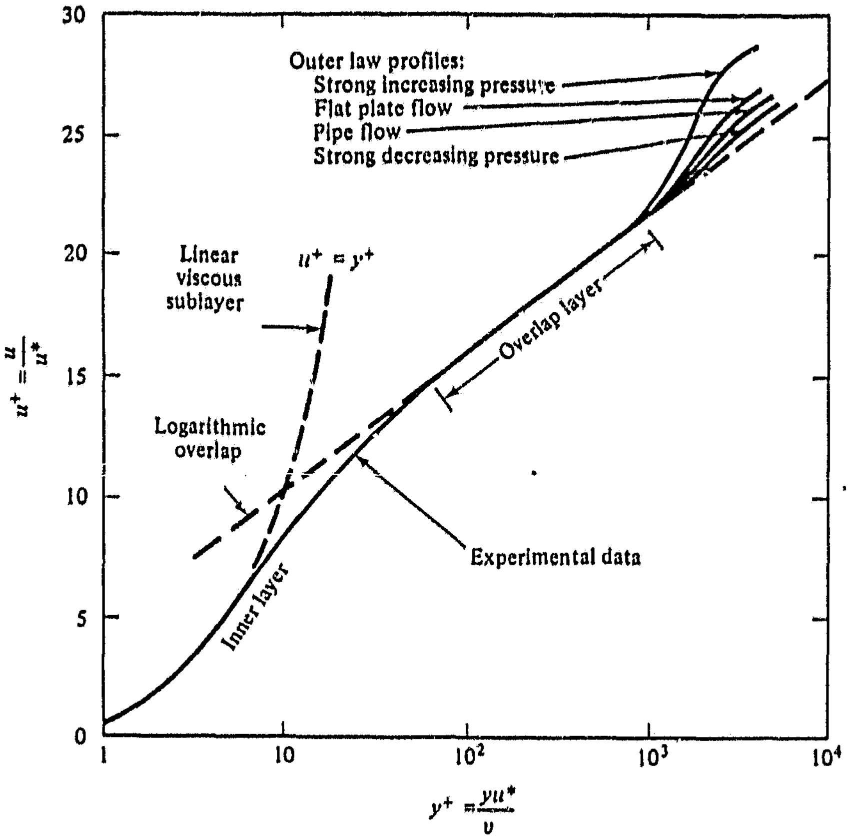

Fig. 3 Experimental verification of the inner-, outer-, and overlap-layer laws relating velocity profiles in turbulent wall flow

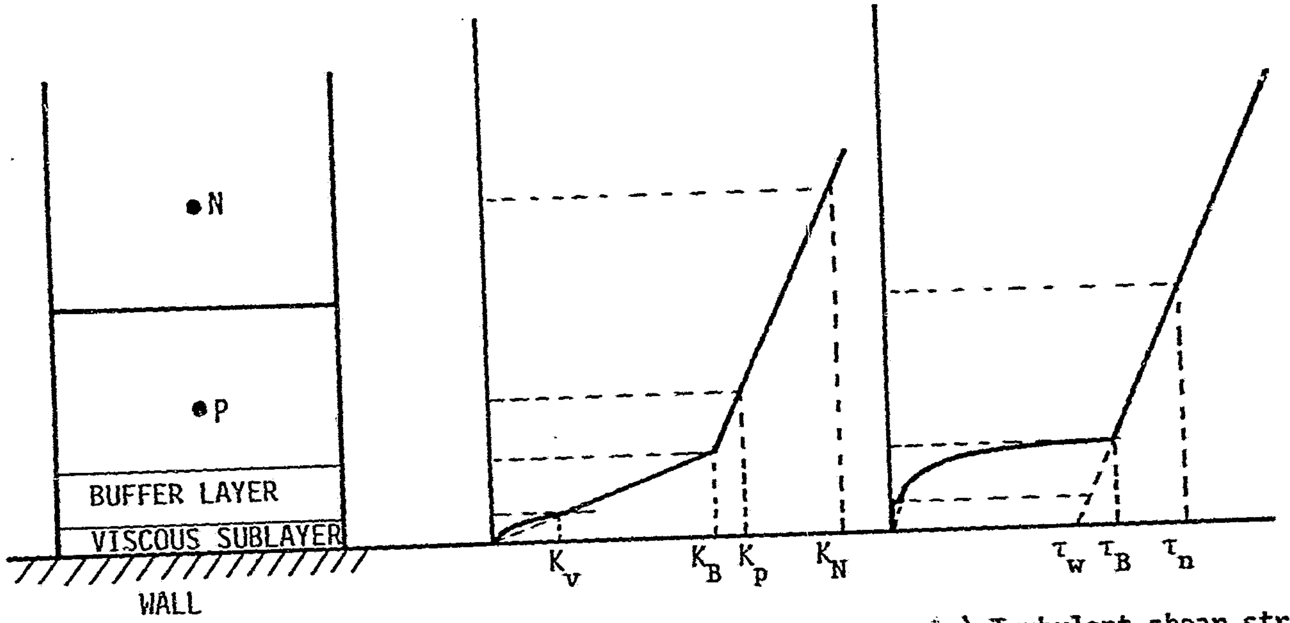

(a) Wall-adjacent cell

(b) Turbulent kinetic energy profile used

(c) Turbulent shear stress profile used

Fig. 4 Near-wall Three-zone Model

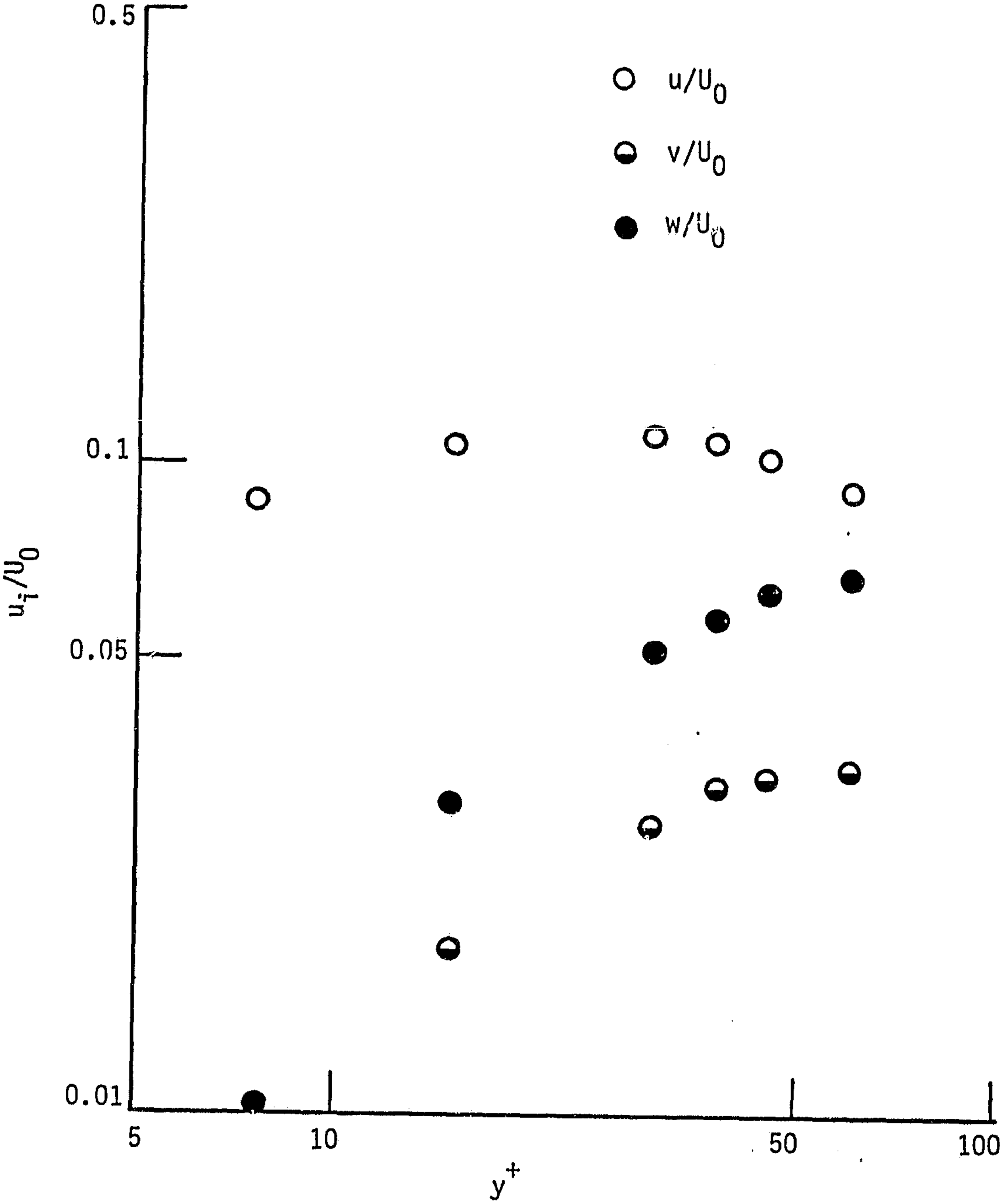

Fig. 5 Experimental data of fluctuating velocities near the wall (data in ref.[8])

ORIGINAL PAGE IS
OF POOR QUALITY

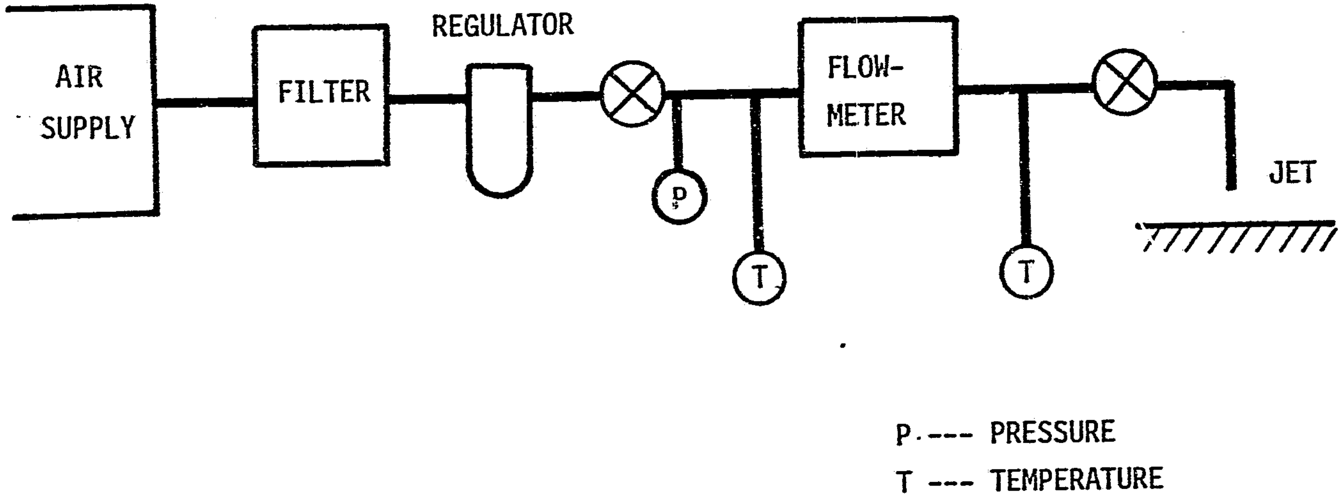

Fig. 6 Experimental Set Up of Turbulent Impinging Jet on a Flat Plate

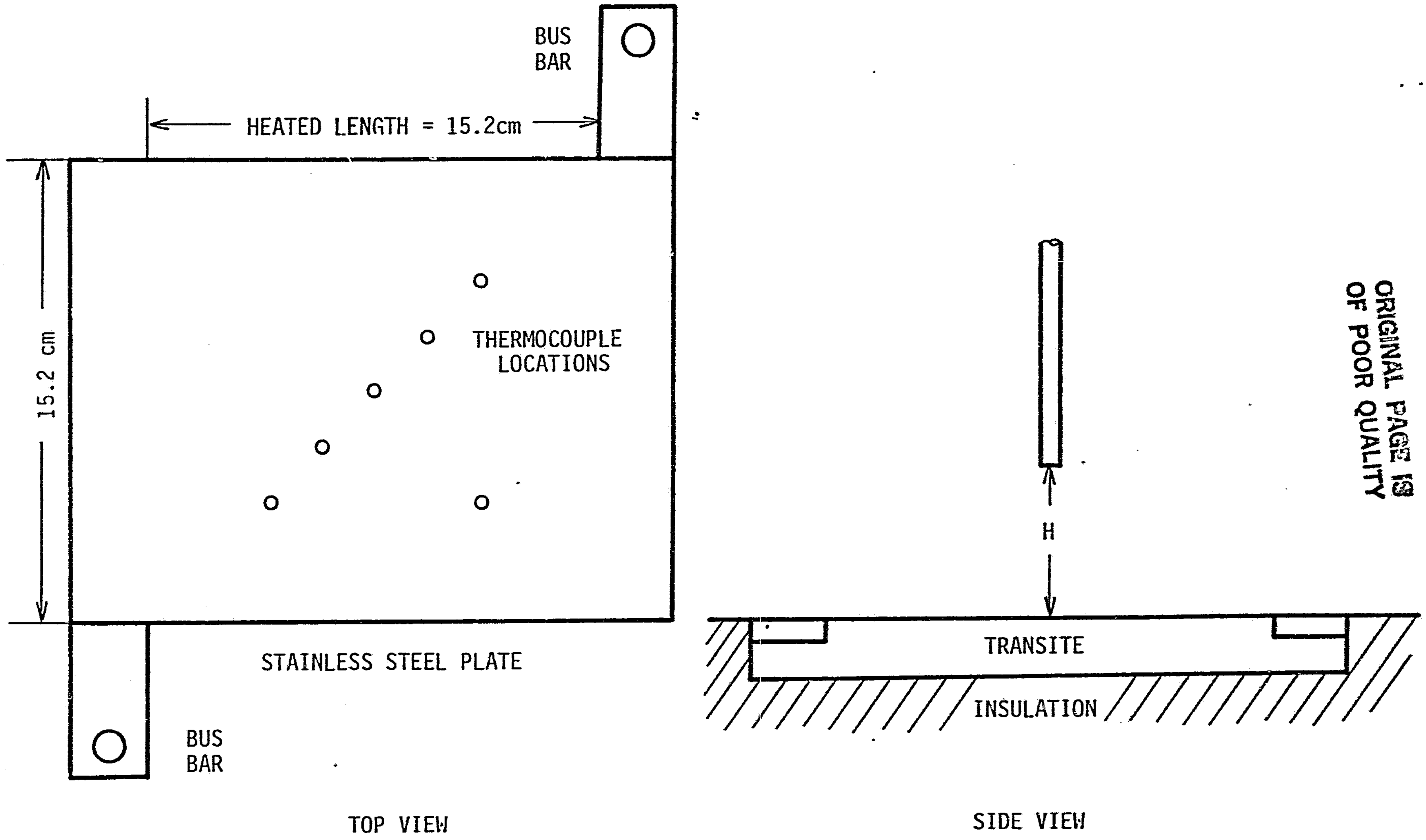

Fig. 7 Test Section of Turbulent Impinging Jet on a Flat Plate

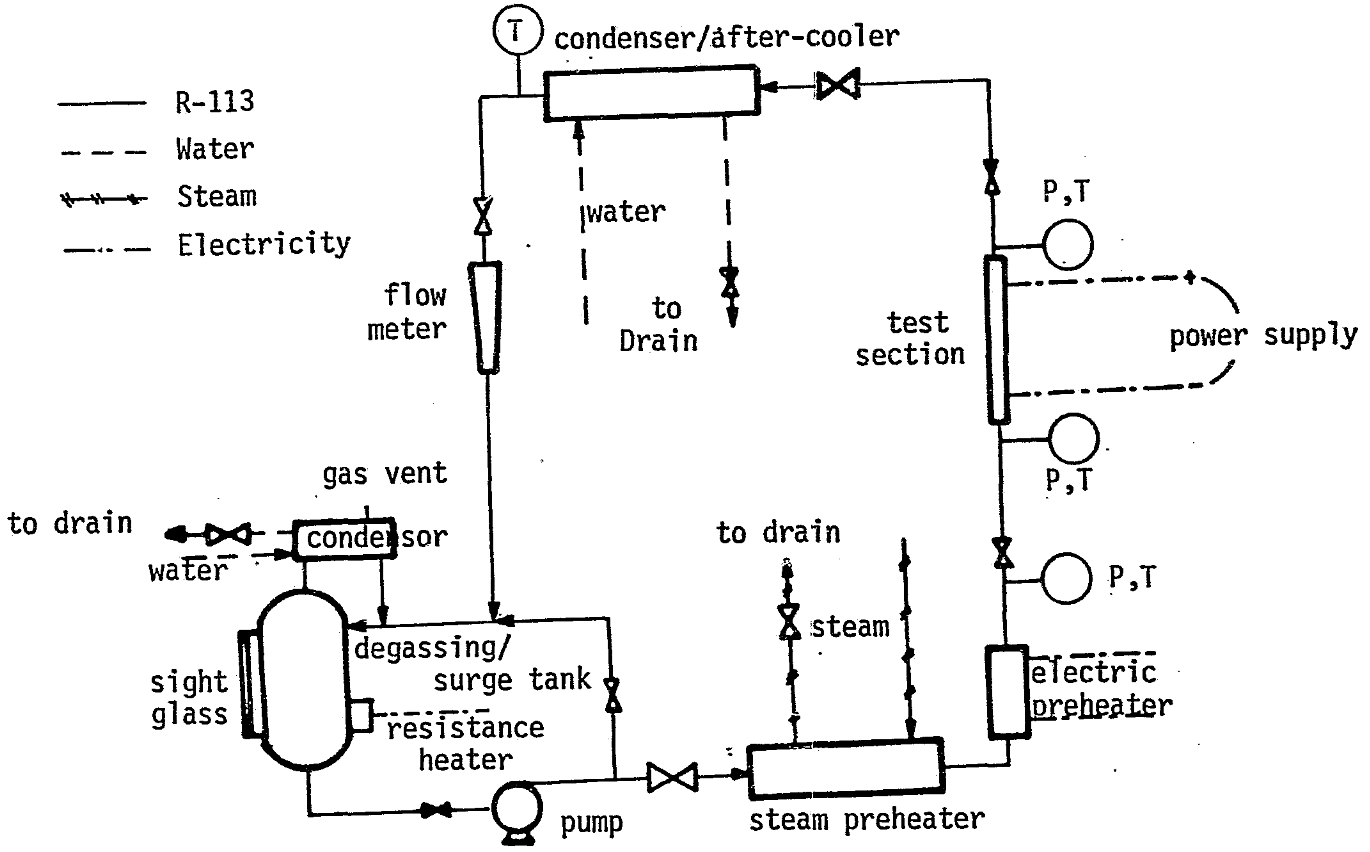

Fig. 8 Schematic Layout of Test Loop of Turbulent Flow in a Circular Pipe with an Abrupt Expansion

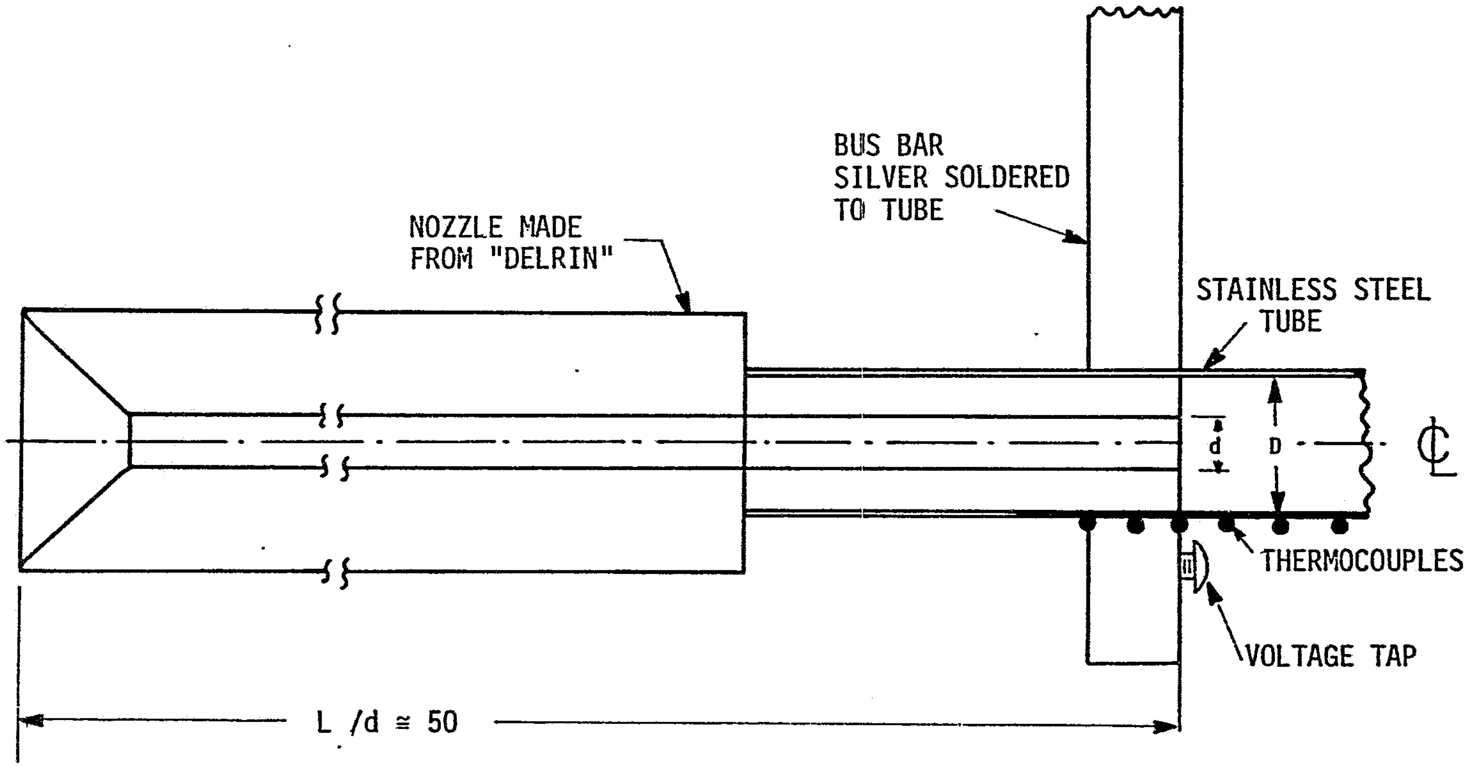

Fig. 9 Details of Abrupt Expansion Assembly (Not to Scale)

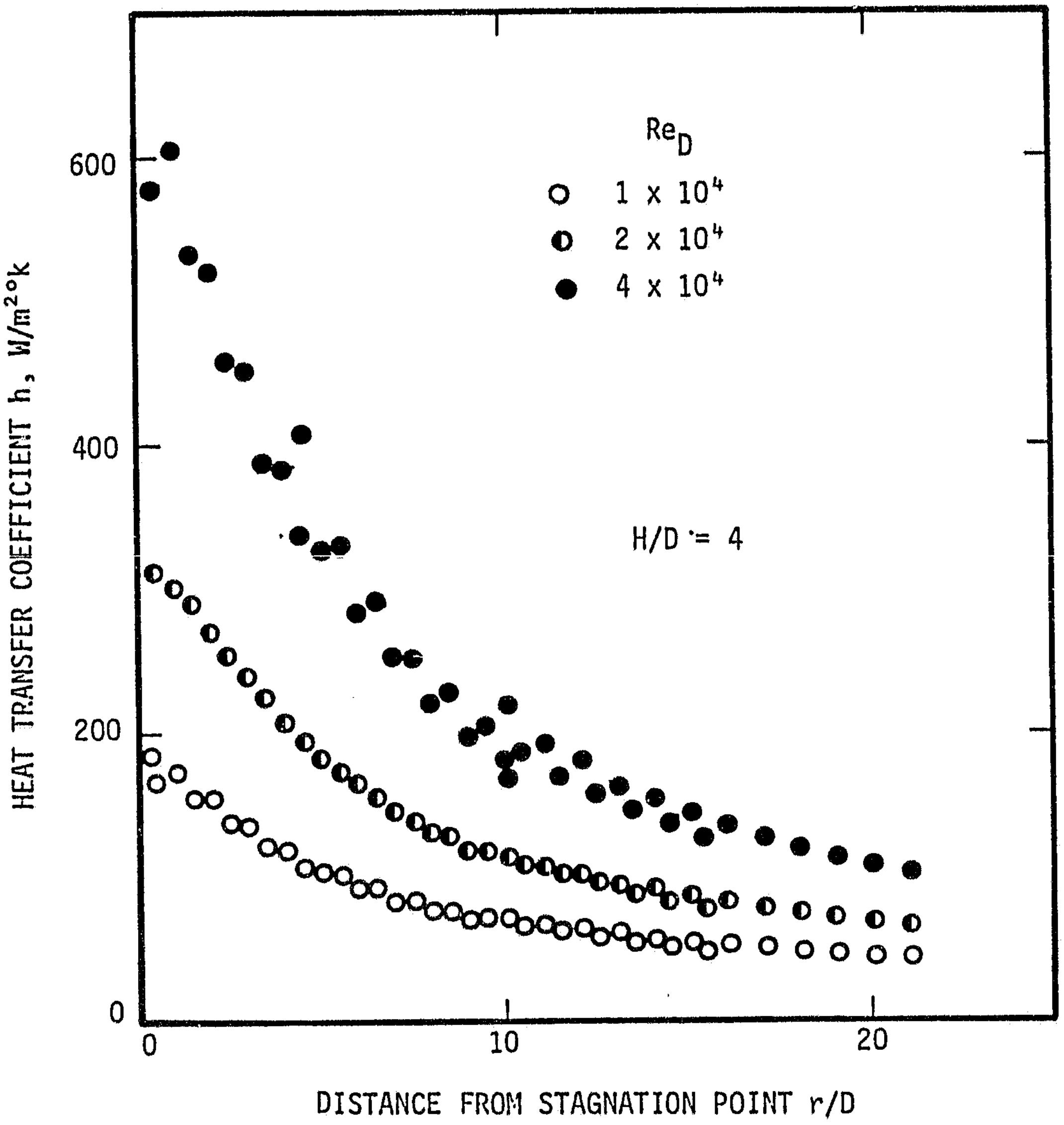

Fig. 10 Experimental Results of Heat Transfer Coefficient along a Flat Plate for Turbulent Impinging Jets

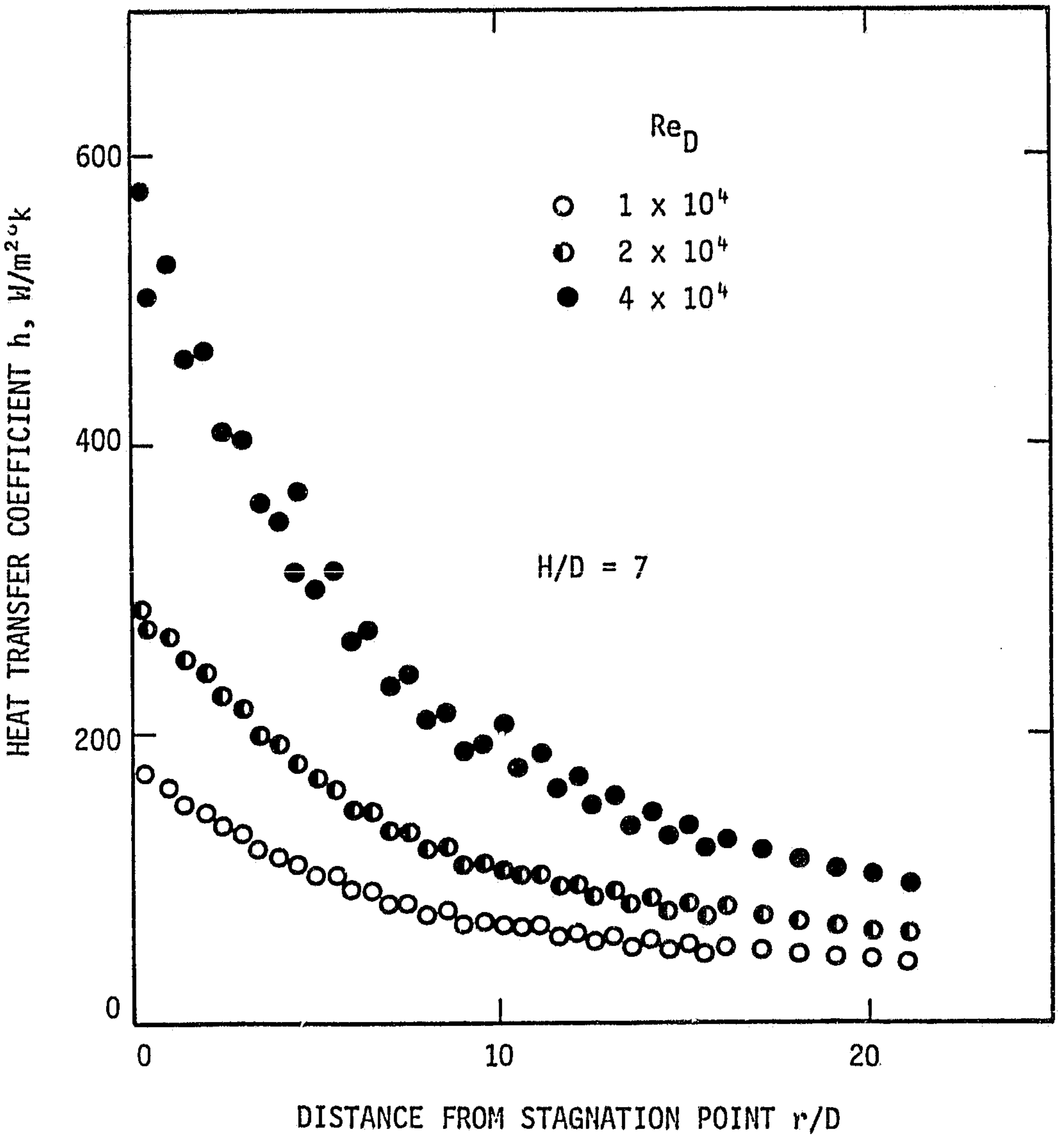

Fig. 11 Experimental Results of Heat Transfer Coefficient along Flat Plate for Turbulent Impinging Jets

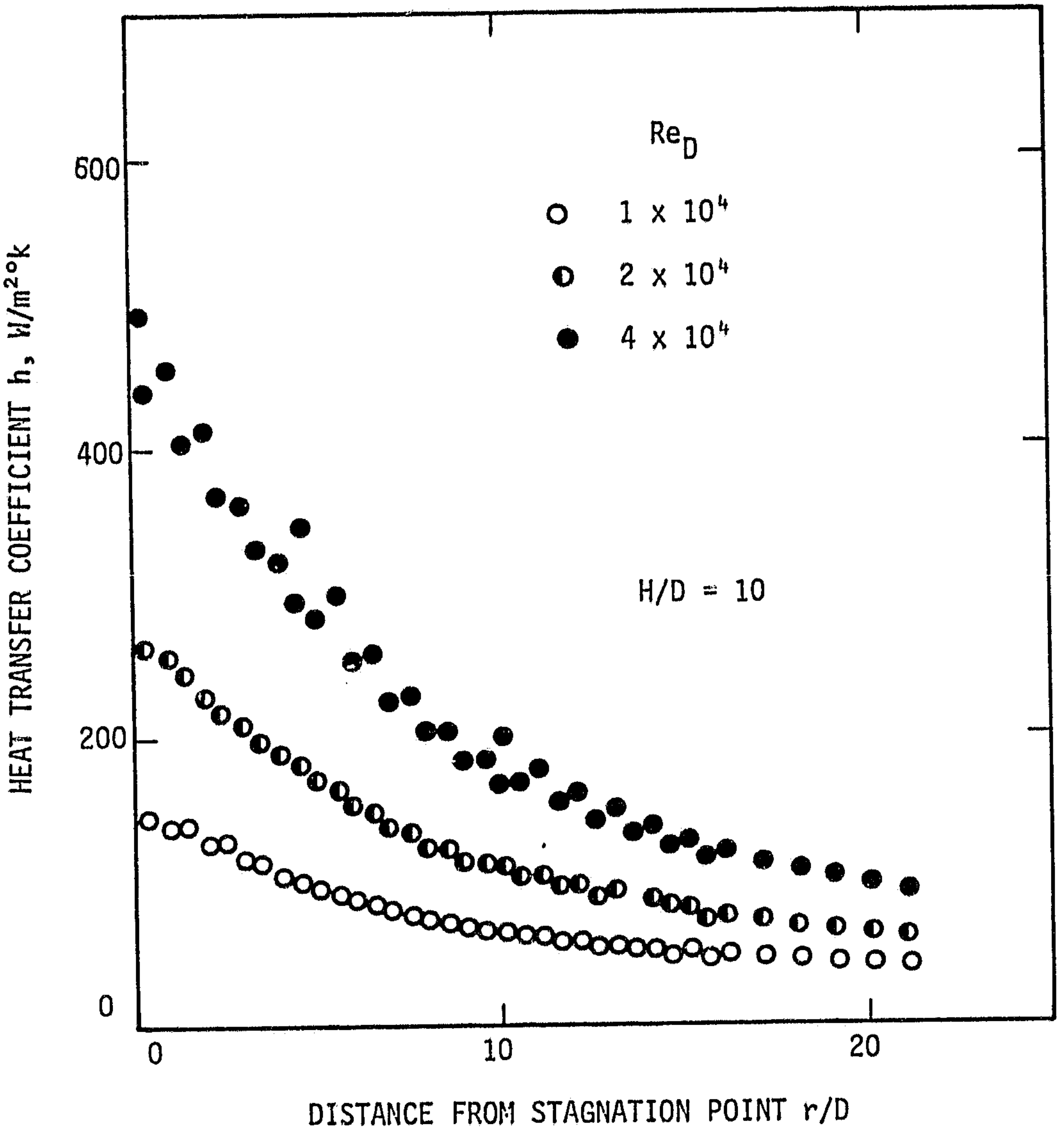

Fig. 12 Experimental Results of Heat Transfer Coefficient along a Flat Plate for Turbulent Impinging Jets

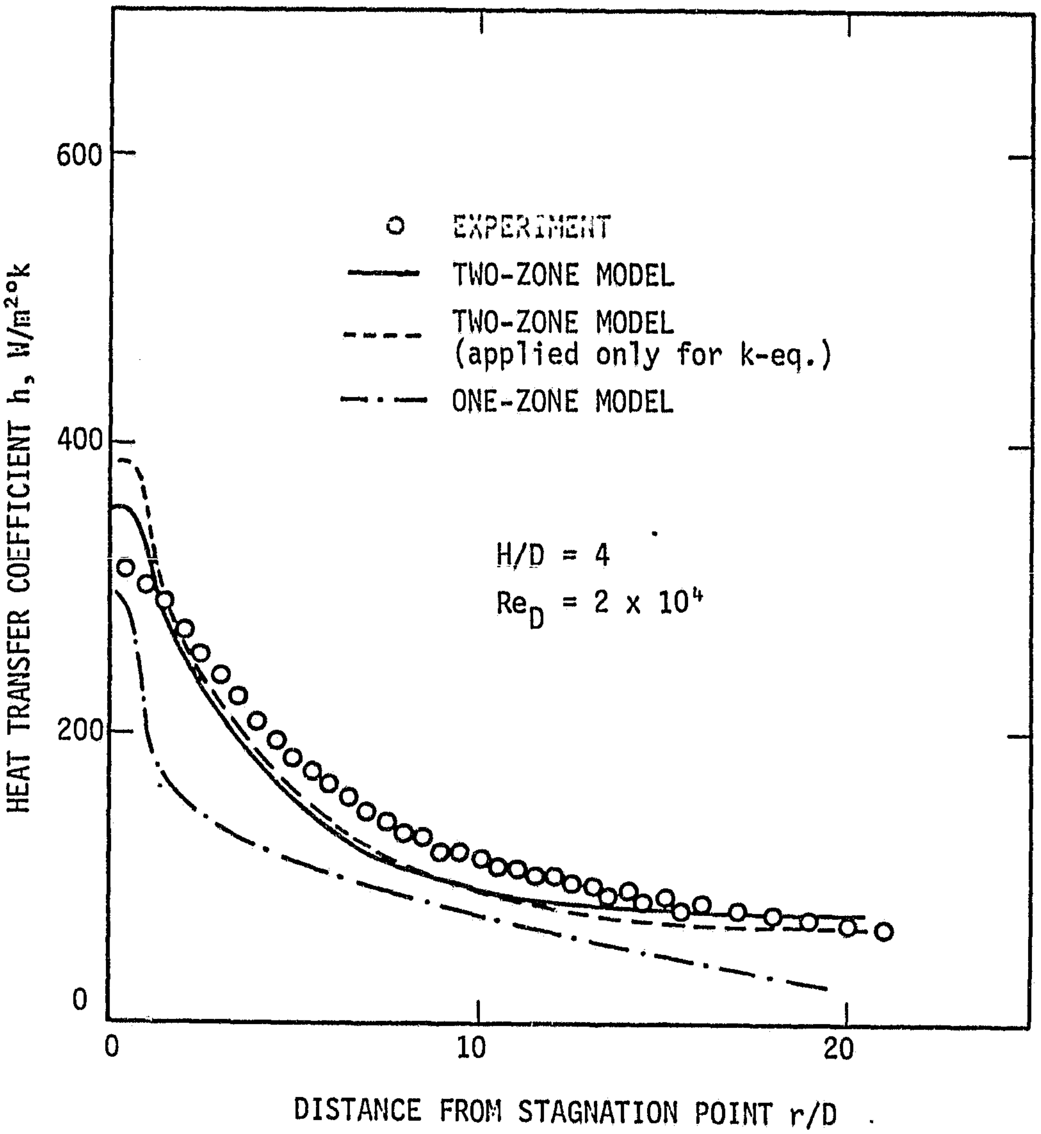

Fig. 13 Heat Transfer Coefficients along a Flat Plate for Turbulent Impinging Jets

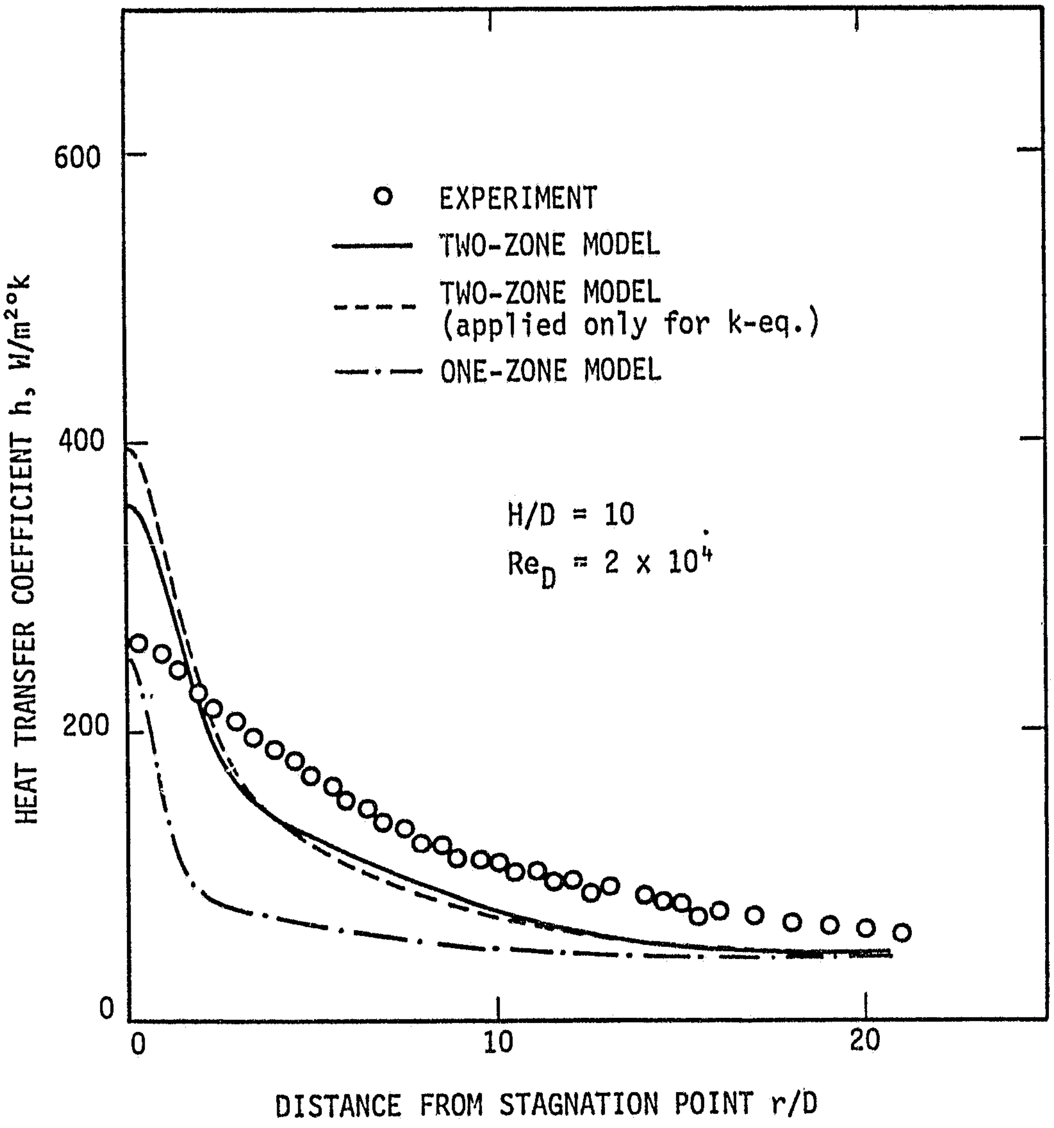

Fig. 14 Heat Transfer Coefficients along a Flat Plate for Turbulent Impinging Jets

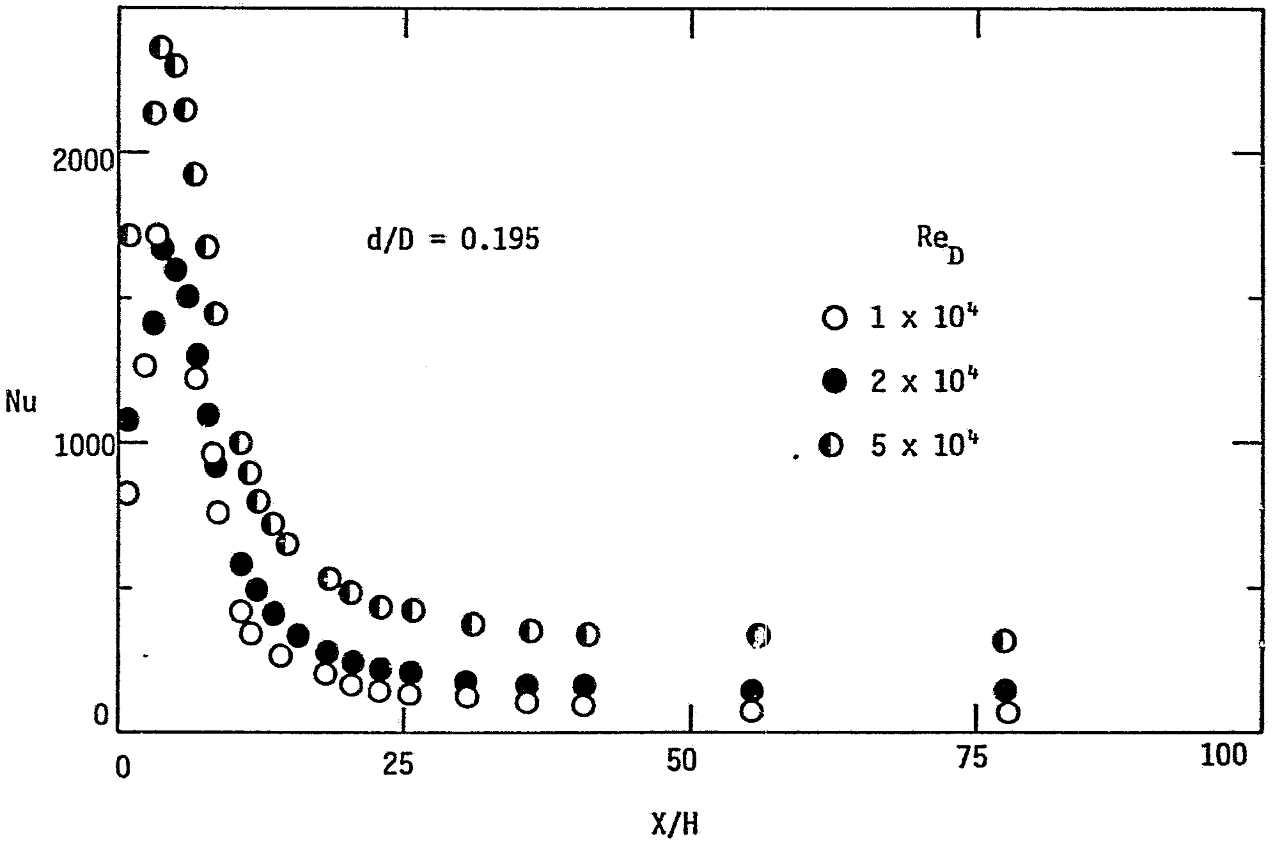

Fig. 15 Experimental Results of Nusselt Number Distribution for Turbulent Flows in a Pipe with an Abrupt Pipe Expansion

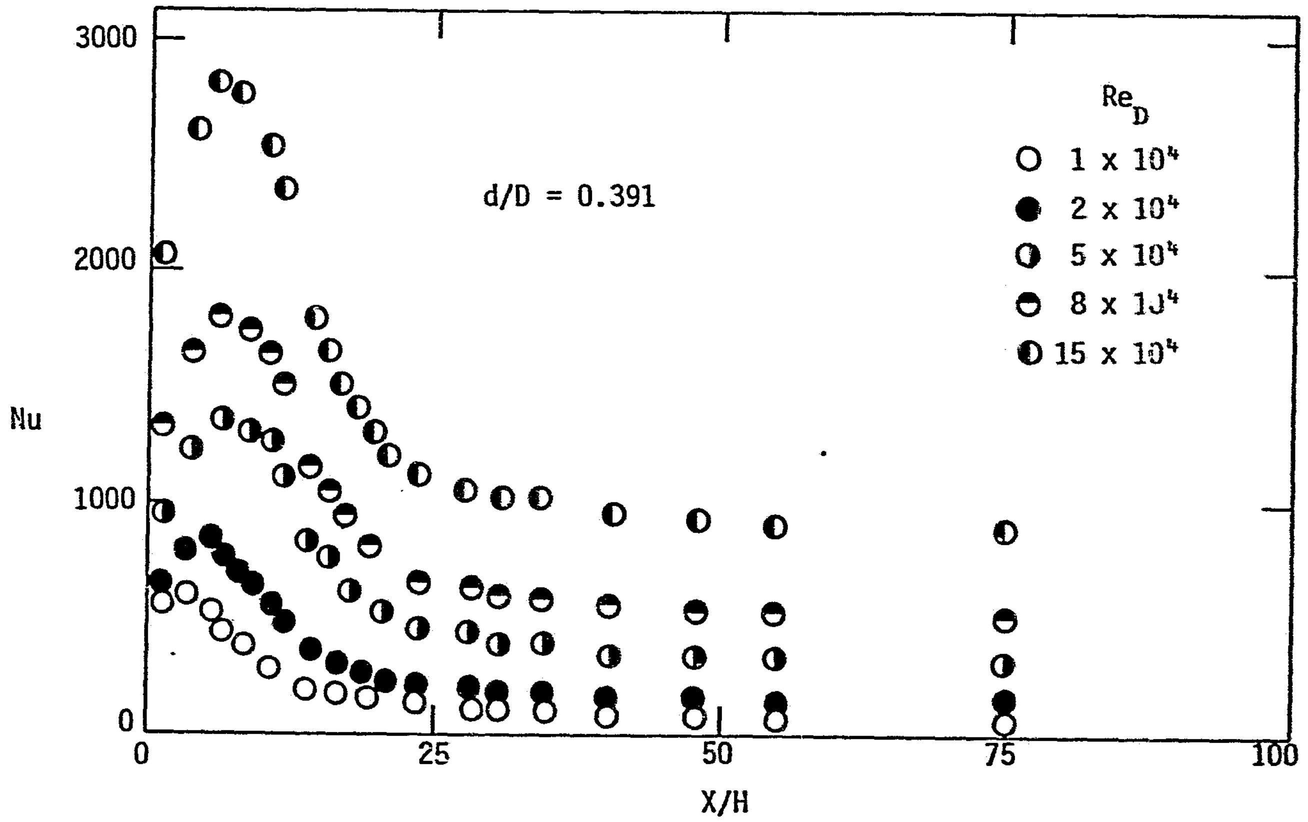

Fig. 16 Experimental Results of Nusselt Number Distribution for Turbulent Flows in a Pipe with an Abrupt Pipe Expansion

ORIGINAL PAGE IS
OF POOR QUALITY

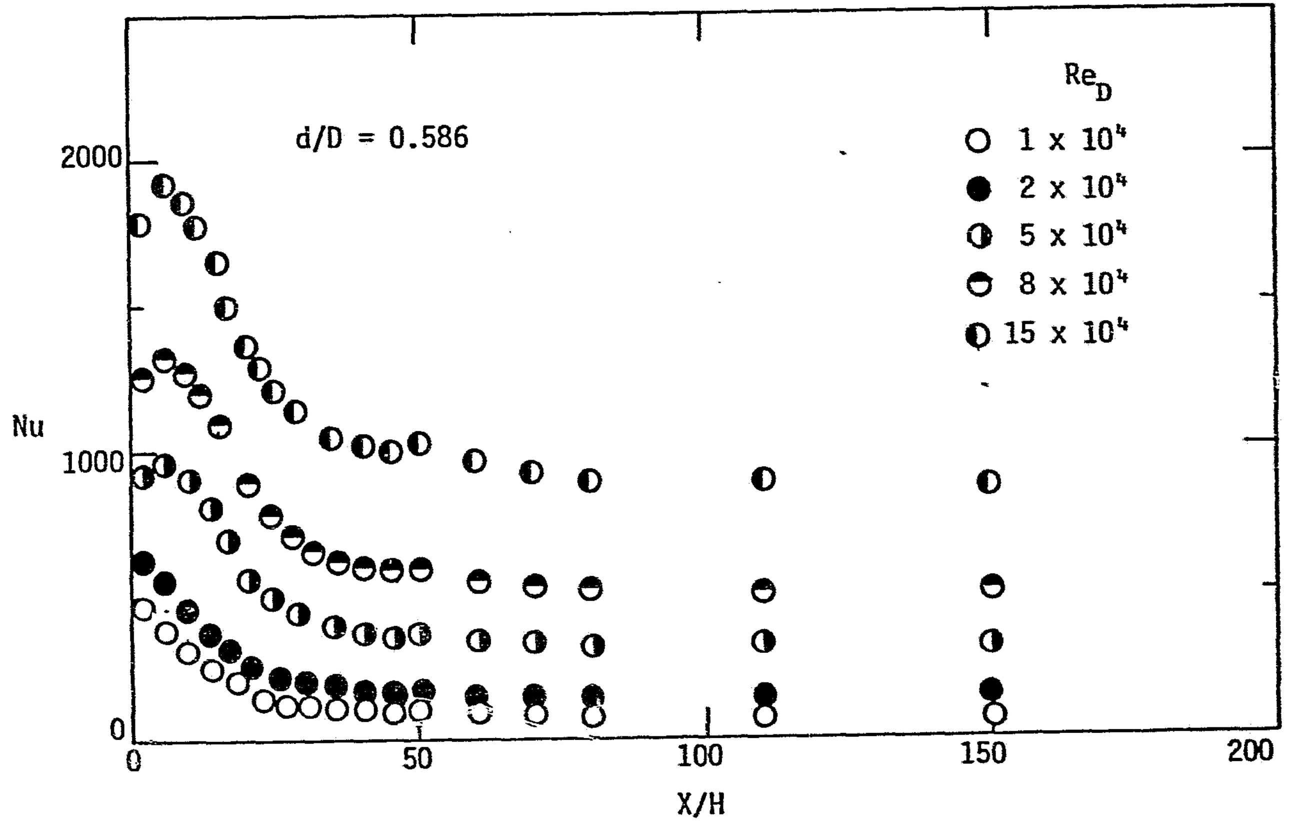

Fig. 17 Experimental Results of Nusselt Number Distribution for Turbulent Flows in a Pipe with an Abrupt Pipe Expansion

ORIGINAL PAGE IS
OF POOR QUALITY

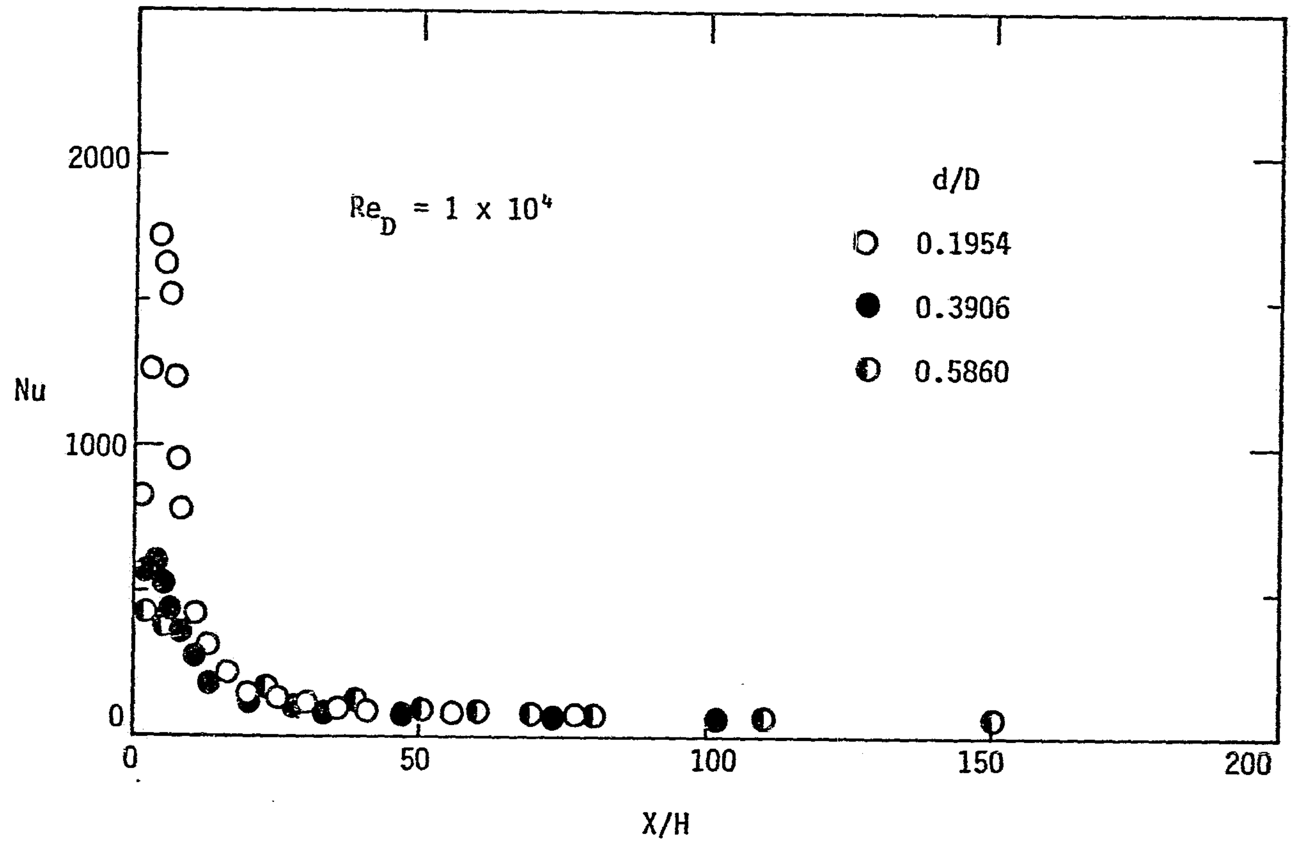

Fig. 18 Experimental Results of Nusselt Number Distribution for Turbulent Flows in Pipes with an Abrupt Pipe Expansion

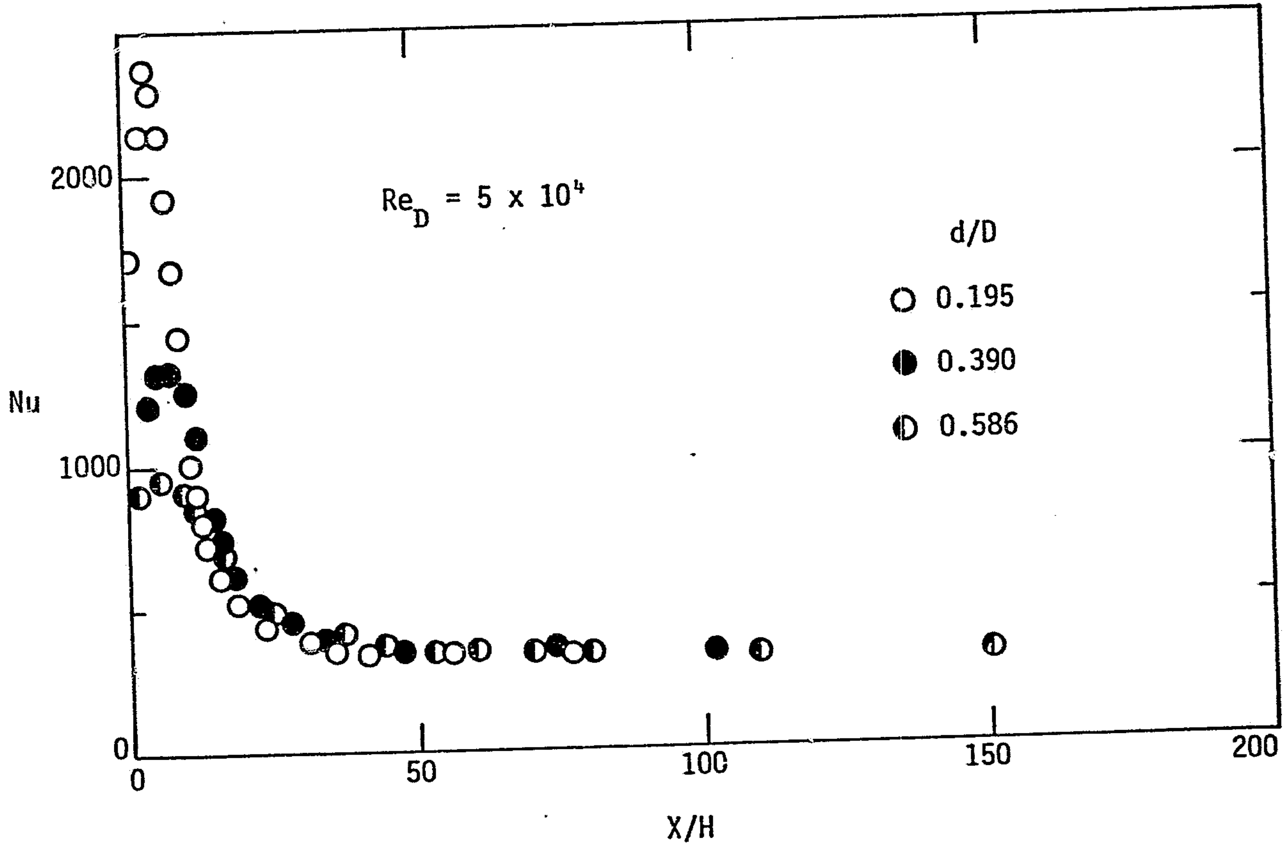

Fig. 19 Experimental Results of Nusselt Number Distribution for Turbulent Flows in Pipes with an Abrupt Pipe Expansion

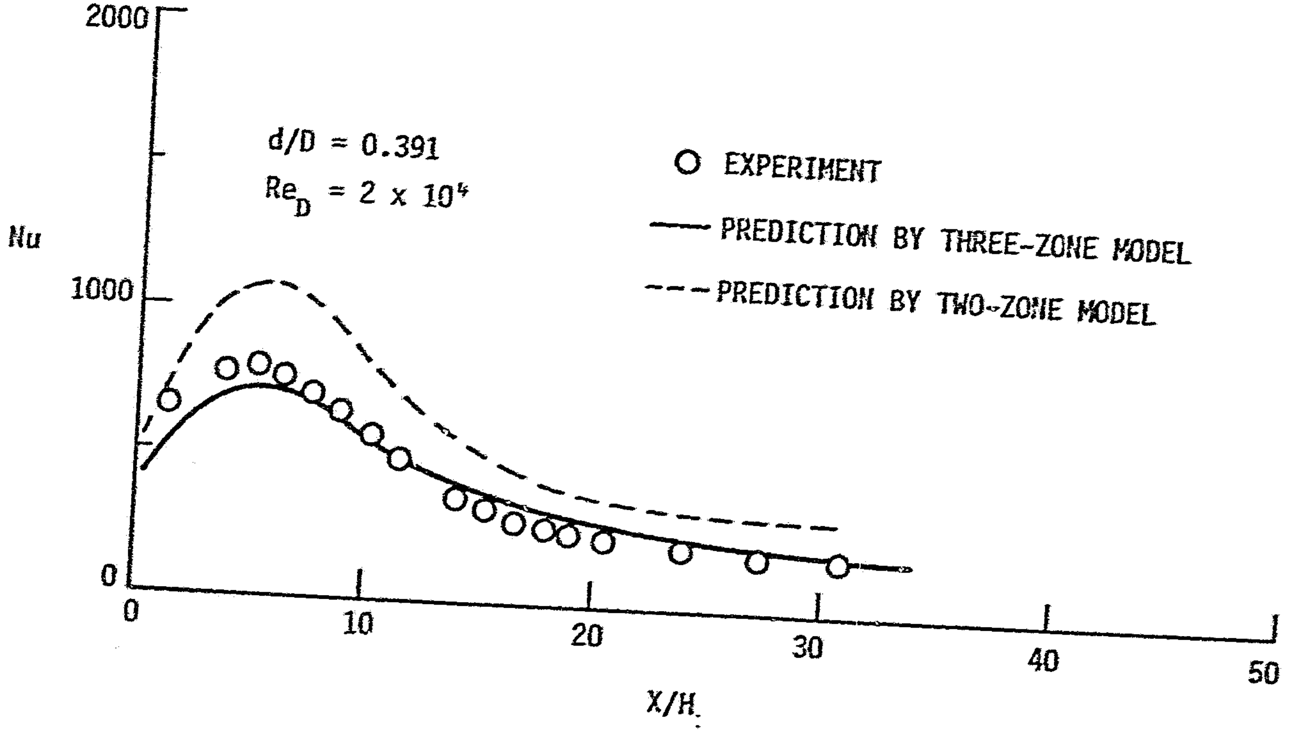

Fig. 20 Nusselt Number Distribution for Turbulent Flow in a Pipe with an Abrupt Pipe Expansion

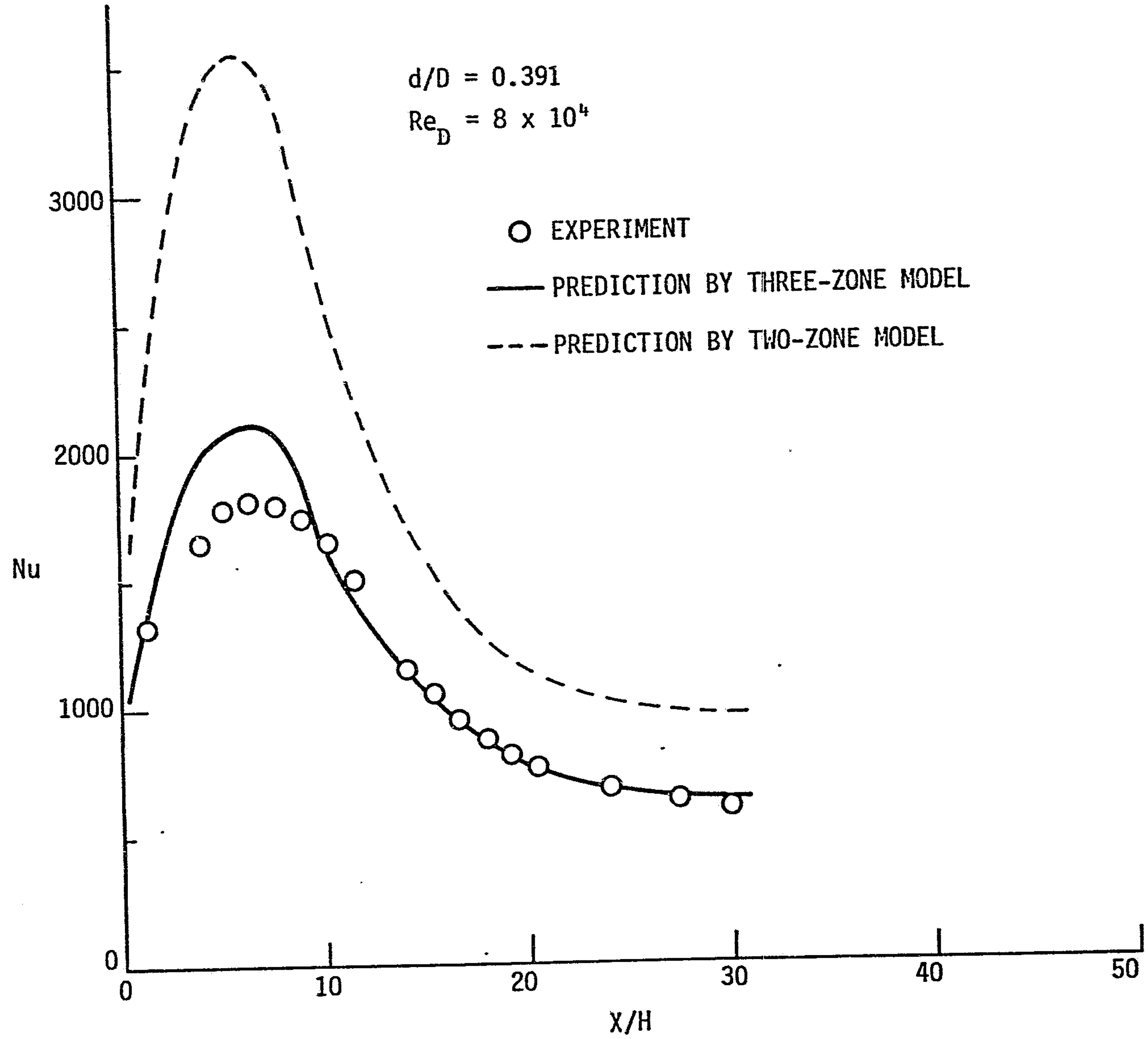

Fig. 21 Nusselt Number Distribution for Turbulent Flow in a Pipe with an Abrupt Pipe Expansion

ORIGINAL PAGE IS OF POOR QUALITY

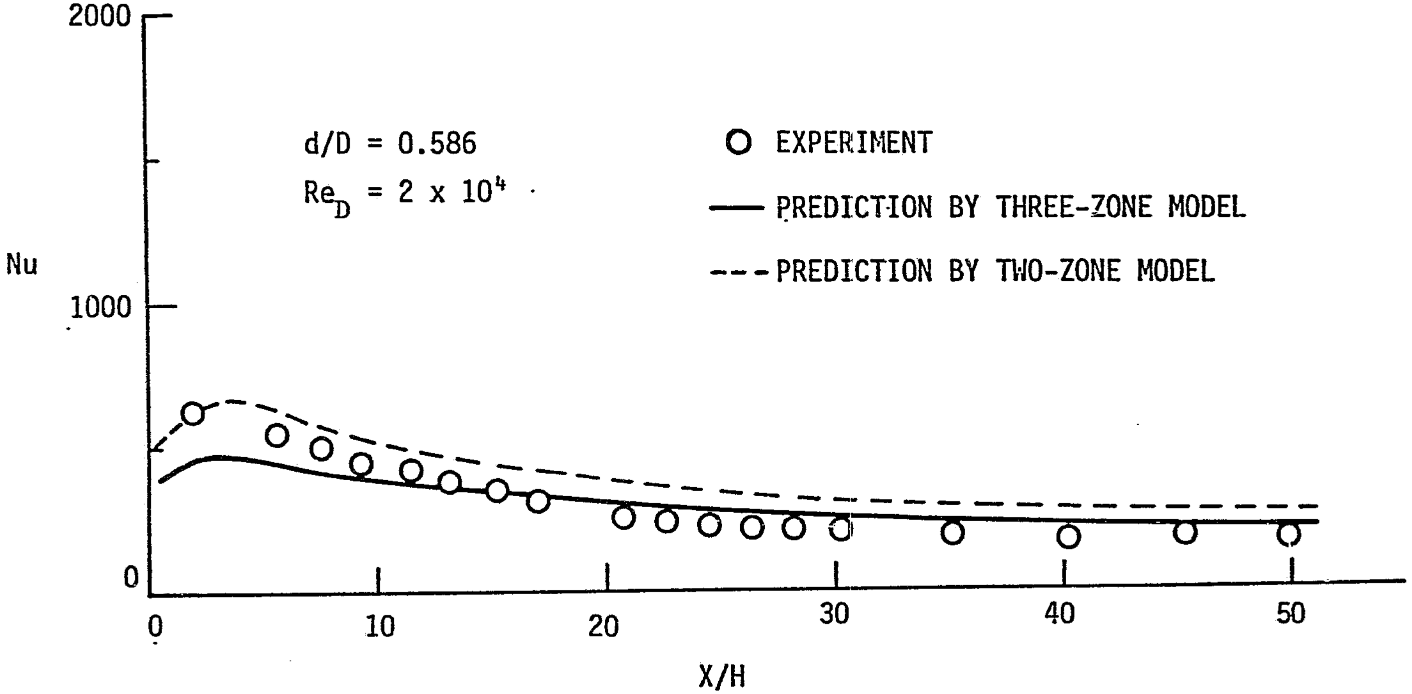

Fig. 22 Nusselt Number Distribution for Turbulent Flow in a Pipe with an Abrupt Pipe Expansion

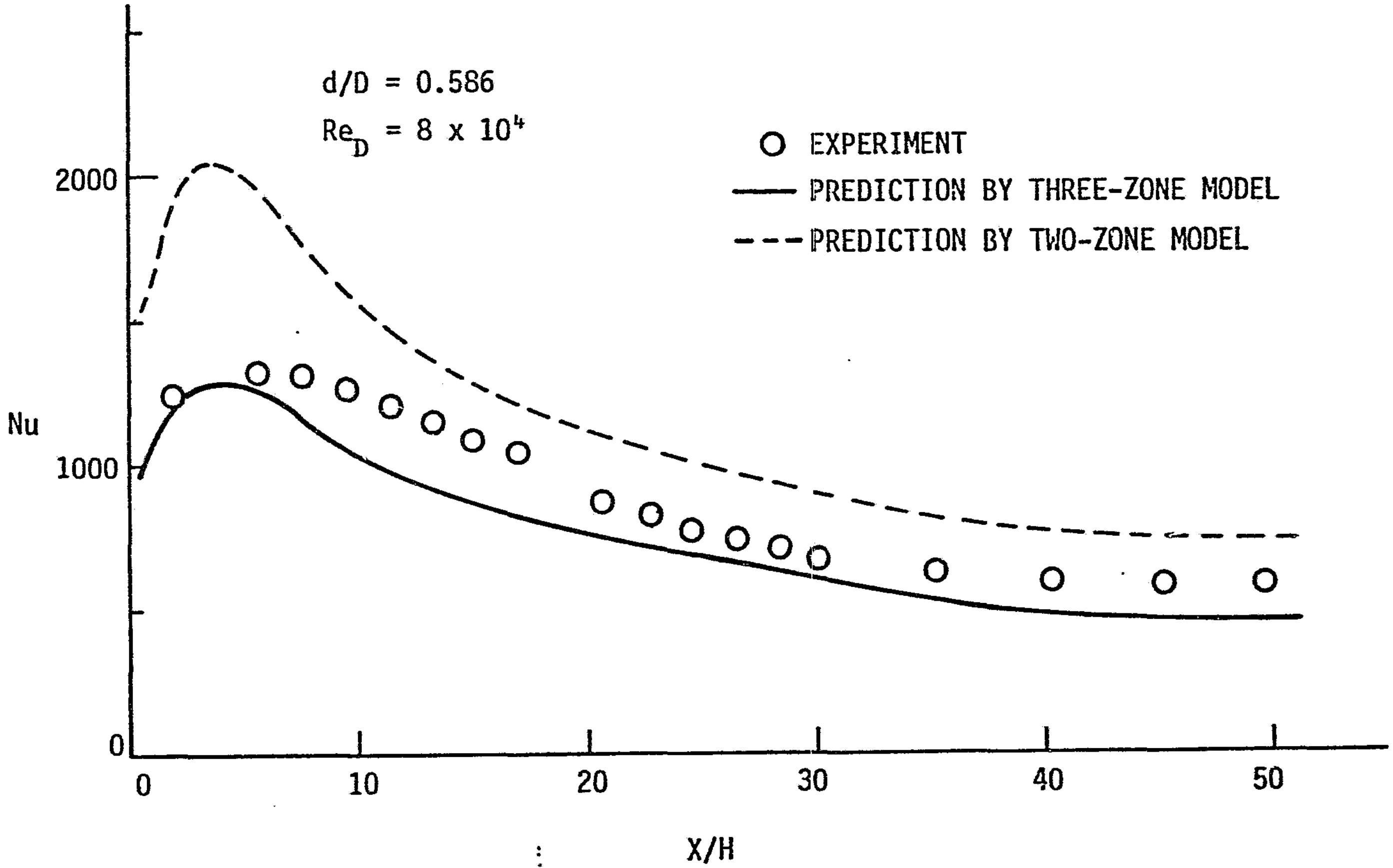

Fig. 23 Nusselt Number Distribution for Turbulent Flow in a Pipe with an Abrupt Pipe Expansion